Quasigeostrophic Forecasting and Physical Processes of Iceland–Faroe Frontal Variability

ARTHUR J. MILLER,* HERNAN G. ARANGO,** ALLAN R. ROBINSON,** WAYNE G. LESLIE,**
PIERRE-MARIE POULAIN,* AND ALEX WARN-VARNAS*

*SACLANT Undersea Research Centre, La Spezia, Italy
** Division of Applied Sciences and Department of Earth and Planetary Sciences, Harvard University, Cambridge, Massachusetts

ABSTRACT

Using a hydrocast survey of the Iceland–Faroe Front (IFF) from October 1992, quasigeostrophic forecasts are studied to validate their efficacy and to diagnose the physical processes involved in the rapid growth of a cold tongue intrusion. Explorations of 1) the choice of initial objective analysis parameters, 2) the depth of the unknown level of no motion, 3) the effects of surrounding mesoscale activity, 4) variations in the boundary conditions, and 5) simple assimilation of newly acquired data into the forecasts are carried out.

Using a feature validation technique, which incorporates a 1) validating hydrocast survey, 2) satellite SST images, and 3) surface drifter observations, most of the forecasts are found to perform well in capturing the key events of the validation strategy, particularly the development of the cold tongue intrusion (though it tends to develop somewhat more weakly and slightly farther downstream than observed). Sharp resolution of frontal structure (to capture seed anomalies in the IFF, which later can grow to large amplitude) and smooth representation of far-field boundary conditions (to eliminate spurious persistent inflow/outflow at the boundaries, which can corrupt developing interior flows) are found to be crucial in generating good forecasts.

An analysis of the potential and kinetic energy equations in the region of the developing cold tongue intrusion reveals a clear signature of baroclinic instability. Topography has little influence on this particular instability event because it tends to be surface intensified and occurs rapidly over a timescale of 3–5 days.

1. Introduction

The complicated eddy and frontal evolution in the Iceland–Faroe Frontal (IFF) region has been increasingly documented via observations (e.g., Hansen and Meincke 1979; Smart 1984; Scott and McDowall 1990; Hopkins 1991; Niiler et al. 1992; Perkins 1992; Allen et al. 1994). The region contains a high degree of dynamical mesoscale activity exhibited by frontal meanders and warm and cold eddies with typical space scales of 10–50 km and timescales on the order of a few days. The small space and time scales present a challenge for field measurements and interpretations. Because of the few extensive time series of synoptic observations (e.g., the XBT surveys discussed by Denbo and Robinson 1988a), the physical processes involved in the establishment of this frontal eddy field have been difficult to ascertain. One can turn to numerical models of the IFF (e.g., Maskell et al. 1992) for indications of what controls the frontal meanderings and the growth of mesoscale eddies, but the models are difficult to validate, again because of the paucity of extensive data. Using a combination of data and models, however, can provide complementary information for improving the interpretation of datasets and model integrations.

During October 1992, a dense hydrographic survey of the IFF was conducted by SACLANTCEN and Harvard University, with central goals of using the dataset (along with surface drifter and satellite SST images) for validating IFF dynamical forecasting models and for diagnosing IFF dynamics. Using this dataset, we address here two aspects of modeling IFF variability. To what extent can quasigeostrophic (QG hereafter) models be useful in modeling and forecasting IFF variations? What are the dominant physical processes involved in the growth of eddies in the IFF? By initializing QG forecasting models with data and by verifying forecast fidelity, we herein use the evolving IFF model fields for diagnostic calculations of eddy dynamics, thereby addressing both questions.

In the next section, we present the QG model used in this study. In section 3, we give a more detailed discussion of the datasets and the initialization and validation procedures. Section 4 discusses the results of real-time shipboard forecasting and hindcasting during October 1992, and section 5 contains the results of extensive postcruise forecasting trials in which we explore the effects of initial conditions, boundary conditions, topography, and model framework on the quality of the forecasts. Using the most realistic of the

---

Corresponding author address: Dr. Arthur J. Miller, Climate Research Division, SIO-UCSD, La Jolla, CA 92093-0224.

forecasts, in section 6 we diagnose the physical processes leading to the dominant frontal instability event seen in the dataset. Our results are summarized in section 7.

2. Forecasting model

Forecasting[1] of open-ocean mesoscale eddy fields over weekly timescales is of considerable interest in a variety of civilian and military applications (e.g., Mooers et al. 1986; Peloquin et al. 1992). Much progress has been made in the practical application of QG models to this end (e.g., Robinson 1992), with particular success in open ocean regions with relatively flat topography.

In oceanic locations with steep topographic variations and strong density fronts, such as the IFF, one might fear that short-term quasigeostrophic forecasting would fail if topography exerts a strong influence on the instability processes of mesoscale variability or if frontal dynamics are severely ageostrophic. Since shipboard forecasting is facilitated with forecasting models that are simple (in initialization strategy, computational demands, and interpretation of results), we seek to determine in this study the extent of the usefulness of QG forecasting models in the IFF. Progress in this direction was made previously by Denbo et al. (1988) and Denbo and Robinson (1988a,b), who studied QG forecasts initialized with lower resolution datasets.

The Harvard Open Ocean Quasigeostrophic Model (Haidvogel et al. 1980; Miller et al. 1981; Robinson and Walstad 1987; Özsoy et al. 1992) was used as the forecasting tool in all the experiments to be described. The topography of the area varies from less than 300 m in some regions to more than 1000 m in others. We decided to use 700 m as the representative total depth of the QG model. Based on an optimum representation of the vertical modes calculated from a previous (June 1989) CTD dataset in the area (W. Leslie 1992, personal communication), a five-layer model was constructed with layer depths of 100 m, 100 m, 100 m, 200 m, and 200 m. The domain was chosen to contain the tracks followed by the ship during the cruise (Fig. 1), with the central grid point at (64.25°N, 10.5°W), a grid of 43 × 37 points, and 5-km resolution. No external wind forcing was included, so the fundamental assumption is that internal ocean quasigeostrophic instability processes control the evolution of the flow field. High wavenumber damping was specified through the use of a Shapiro filter (see Miller et al. 1981), with parameters FIL = (4, 2, 1) for the bulk of the experiments discussed below, indicating an eighth-order Laplacian damping applied twice per time step. Although

the large topographic variations in the domain certainly could violate the quasigeostrophic approximation, topographic steering can preserve the quasigeostrophic assumption (Millif and Robinson 1992; Spall and Robinson 1990). We therefore included the full effect of a smoothed version of the realistic topography (Fig. 2) in several experiments; the results are at least suggestive of topography's effect in more realistic models.

3. Datasets: Initialization and validation procedure

a. Initialization survey and validation track

During October 1992, the SACLANTCEN Applied Oceanography Group and the Harvard Open-Ocean Forecasting Group surveyed the IFF between 63°30' and 65°00'N, 12°30' and 8°30'W (Fig. 1) over an 8-day period (19–26 Oct.) as described by Poulain (1992). A 24 km by 9 km resolution hydrographic (CTD/XBT/XCTD) survey (Fig. 1a), over the initial 5.5-day period, formed what we consider to be the initial survey for forecasts. A single ship track, which subsequently crisscrossed the front over the final 2.5-day period (Fig. 1b), constitutes our validating survey. Surface drifter observations throughout the hydrocast period and satellite SST images supplement the initialization and validating hydrocasts.

To use the hydrocast data as initial conditions for a QG model forecast, the data were processed in several steps onboard ship in quasi-real time. First, the data were subjectively analyzed and several "bad" casts were identified and extricated from the data. Then, each cast was extended via exponential extrapolation to a depth greater than 600 m, even if this meant extending the cast into the bathymetry. For each cast that did not measure conductivity, from which salinity can be computed directly, we computed the salinity with a model using an average temperature–salinity relation based on the four nearest CTD measurements from a previous (June 1989) CTD survey. By this means, we arrived at a density profile for each "good" cast. Dynamic height was then computed based on selected levels of no motion, nominally 600 or 400 m in the forecasts discussed below. These dynamic height profiles were objectively analyzed (Robinson and Leslie 1985; Carter and Robinson 1987; Robinson and Walstad 1987) onto the 5 km by 5 km model grid, independently for each of the five levels of the QG model. The choice of objective analysis parameters (OAP hereafter) for $(a, b, err) = $ (zero crossing, exponential decay, error) for the assumed autocorrelation function $R(r) = 1 - (r/a)^2 \exp[-(r/b)^2]$ controls the smoothness and precision of the computed objective analysis. Figure 3a shows an example objective analysis of dynamic height at 50 m relative to 400 m (case LV4-1) for OAP = (60, 10, .1). After scaling

---

[1] In this paper, a "forecast" refers to a model run that only uses information (i.e., initial conditions) available up to day 0 of the integration. "Hindcast" refers to a model run that additionally uses information (e.g., boundary conditions) observed after day 0.
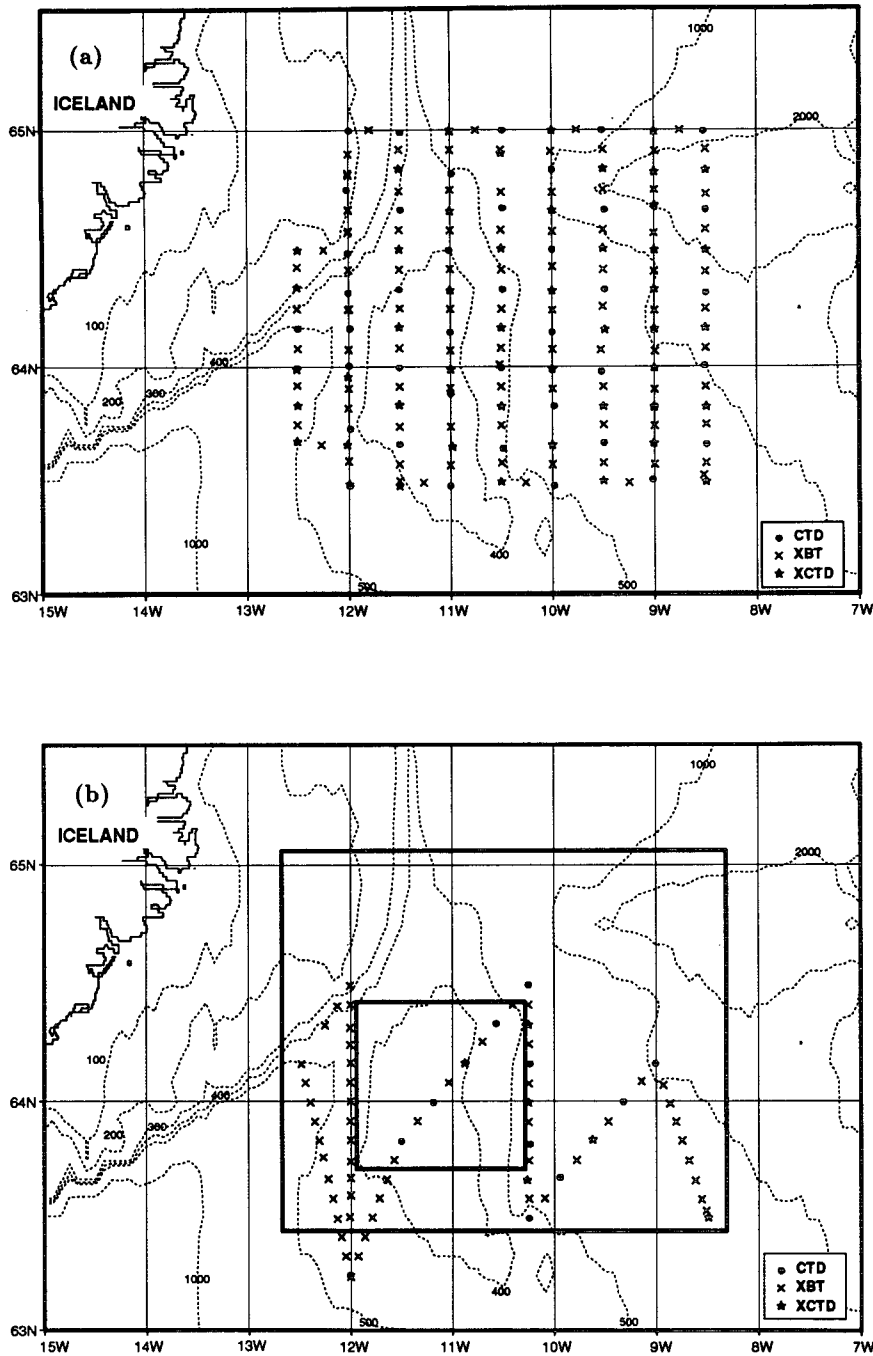
FIG. 1. (a) Locations of the XBTs, XCTDs, and CTDs during the initialization survey. The survey was obtained from west to east from 19 Oct 92 to 24 Oct 92. (b) As in (a) but for the validation track, obtained from east to west from 24 Oct 92 to 26 Oct 92. Topographic contours (m) are shown as dotted lines. Also shown in (b) is the model forecasting domain (large box) and the subdomain (small box) surrounding the developing cold tongue used in the energy budget analysis discussed in section 6.

the dynamic height into streamfunction the fields were input as initial conditions to the QG models discussed in the subsequent sections. After the same manner, the validation survey was transformed into a dynamic height field on the model grid for plotting and intercomparison purposes.
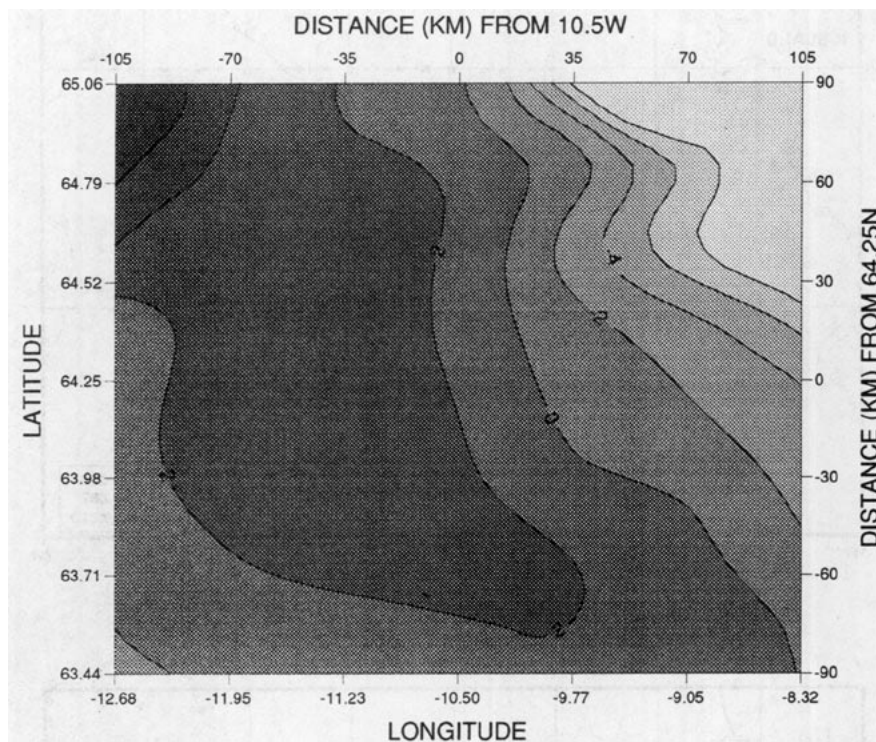
TOPOGRAPHY IN MODEL DOMAIN

FIG. 2. Nondimensional perturbation topography used in some cases for the QG model. The realistic topography was smoothed, then the mean was removed. Contour interval = 2.0 (multiply by 62.5 to redimensionalize to meters). Dimensions of the model forecasting domain in kilometers are also indicated.

b. Validation strategy

1) HYDROCASTS

The validating hydrocast survey (e.g., Fig. 3b) is clearly inadequate for carrying out a statistical validation of QG forecasts. Furthermore, the initialization survey is not synoptic, being gathered over a 5-day period, a timescale comparable to that of the evolving mesoscale eddy field that we seek to predict. Therefore, we decided to use the track as a window through which "events" may be identified in the evolution of the IFF. The objective analysis procedure yields an error field by which we may define our "verification window," the region for which objective analysis error is less than some chosen value in the validating survey. The time differential from the initialization survey to the validation track for each event can then be directly related to a forecast day of a prediction.

Progressing from the beginning of the validation track to the end, we identified three events that occurred (marked in Figs. 3b,c), each at a different time interval from the initial survey time:

F1) *Current disappearance.* The eastward flowing current at 64°10'N, 11°00'W that was evident in the initial survey (21–22 Oct 1992) was not present when

the validation survey crossed that position 3–4 days later (25 Oct 1992).

F2) *Cold tongue intrusion.* A cold tongue intruded into the region 63°70'–64°00'N, 11°30'–12°00'W during the validating survey (25 Oct 1992) compared to four days earlier during the initial survey (21 Oct).

F3) *Northward shift of the front.* The IFF measured along 64°20'N, 12°40'W on 19–20 Oct 1992 shifted northward by roughly 15 km and broadened after 6–7 days when resampled on 26 Oct 1992.

These three events form the basis for our hydrocast feature validation.

Besides these changes, we also note that a cold eddy was located south of the front (63.7°N, 10.5°W) as evidenced in the initial and validating hydrographic surveys as well as the satellite images (e.g., see next paragraph) and drifter tracks (e.g., see Fig. 8a). This cold eddy was resolved by three adjacent hydrographic measurements (one XBT, one XCTD, and one CTD) along the 10.5°W initialization track, and resolved by three other adjacent measurements of the validation track near 10.25°W (two XBTs and one XCTD) three days later. (The rounded shape of the cold eddy contours in Fig. 3 is due to the objective analysis and is not necessarily representative of
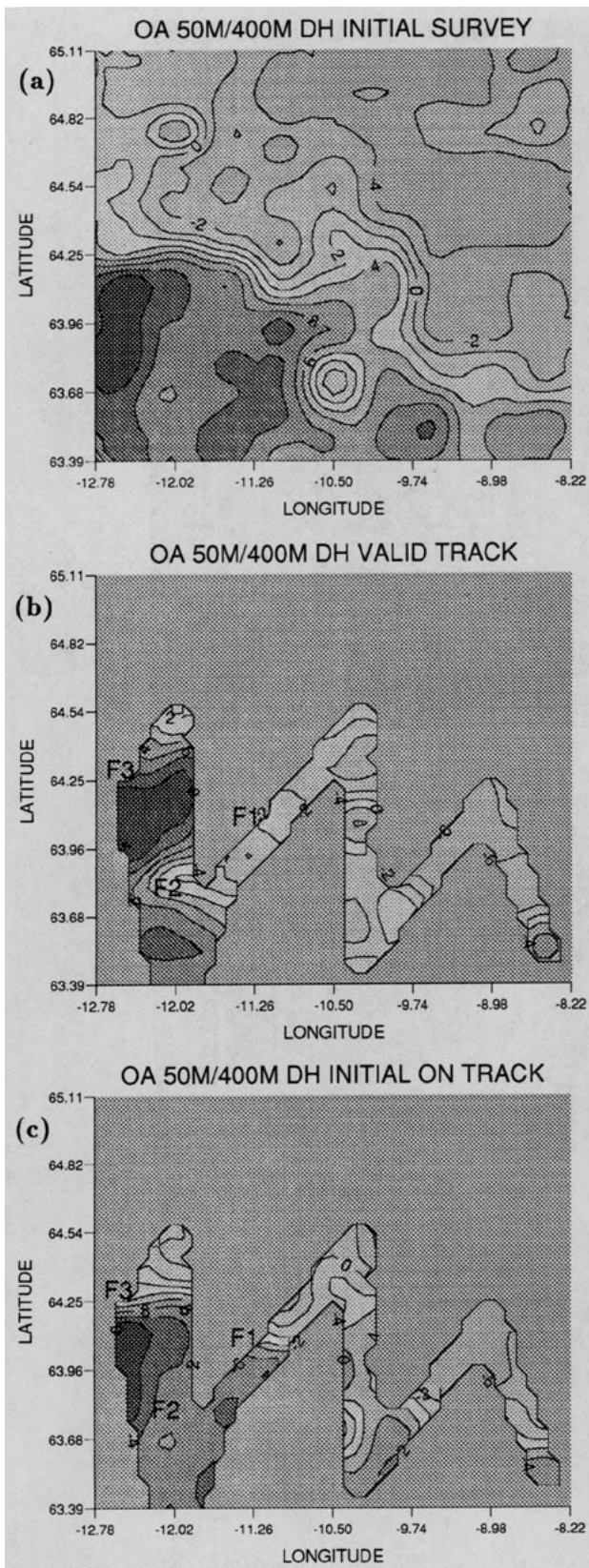
the true cold eddy.) Since none of the six locations where this cold eddy was observed overlap both initial and validation surveys, we can only say (using the hydrographic data alone) that this cold eddy remained nearly in place between our two visits (3-day interval). The satellite images, on the other hand (see next paragraph), indicate that this cold eddy moved slightly eastward in a manner consistent with both initial and validating surveys. Therefore, our forecasts can be further validated by affirming that the cold eddy remains relatively stationary (with slight eastward migration) and stays "isolated" from the IFF current over the first several days of the prediction.

2) SATELLITE IMAGES

Satellite SST images[2] for 16, 19, and 22–24 October serve to corroborate the development of the cold tongue intrusion seen in the validating survey. Although each SST image is partly obscured by cloud cover, these images provide supplemental information to the hydrocast surveys and help to ascertain the degree of synopticity of the initialization survey, especially in the western part of the model domain where the cold intrusion develops.

On 16 October, three days before the hydrocast survey commenced, a satellite SST image (Fig. 4a) shows the IFF possessing a nearly east–west orientation. On 19 October, the day the hydrocast survey began, the SST image (not shown) was mostly blocked by cloud cover, although there is an indication of a slight southward displacement of the front along the western edge of the model domain. On this same day, however, drifter tracks (see next paragraph and Fig. 8a) clearly indicate the continued east–west orientation of the front, similar to the 16 October satellite image and consistent with the hydrocast survey (Fig. 3a). The next usable, though partially obscured, SST image (22 Oct) exhibits a curving IFF at the western edge of the model domain and the image for 23 October shows a partially developed cold tongue extending south to 64°N. On 24 October, the SST image (Fig. 4b) clearly shows the developed cold tongue. From 23 to 24 October, the cold tongue pattern migrates eastward about

---

[2] The satellite images considered in this study come from channel 4 of the AVHRR in the 11-μm infrared band. They have not been corrected for atmospheric effects and do not represent absolute SST fields. For brevity, they are referred to as "SST images" throughout the text.

FIG. 3. Example objective analyses of dynamic height (cm) at 50 m relative to 400 m for case LV4-1. (a) Initial survey, (b) validation track (only the region where the relative error is less than 0.6 is contoured), and (c) initial survey viewed through the error window defined in (b). Contour interval = 2 cm. The locations of the validation features defined in section 3b are indicated by F1, F2, and F3 in (b) and (c). The objective analysis domain is one grid point (5 km) larger than the model forecasting domain on each side.
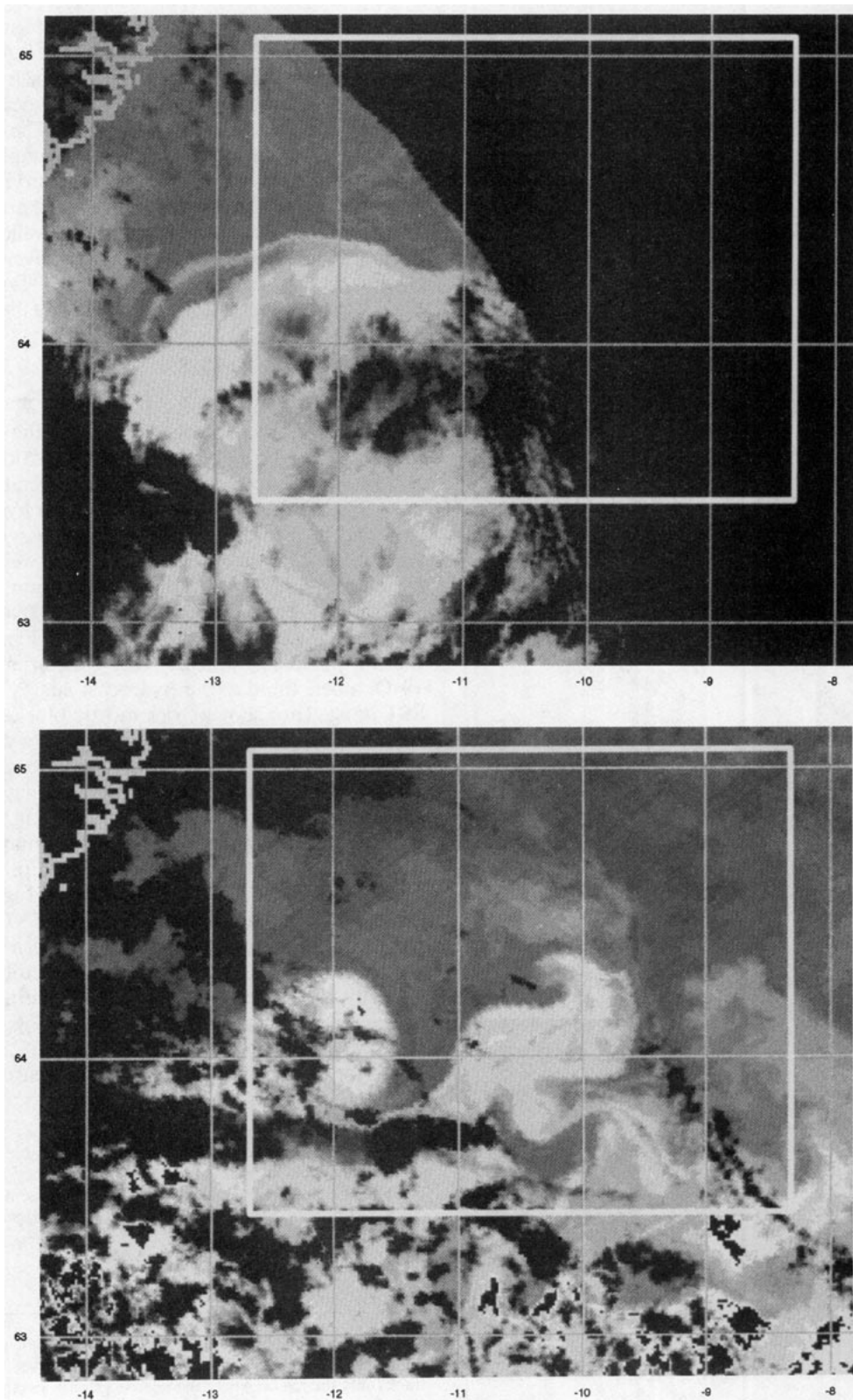
FIG. 4. Satellite infrared (channel 4 of AVHRR) images for (a) 16 Oct. 1992, 1510 UTC and (b) 24 Oct. 1992, 1514 UTC. Black areas indicate clouds, grey areas cooler water, and white areas warmer water. The QG forecasting model domain is traced in each image. Part of the coast of Iceland is delineated in the upper-left corner. The cuspate surface signature of the cold intrusion is clearly evident in (b).

10 km. The cold eddy south of the IFF likewise shifts slightly eastward from 23 to 24 October, though its surface signature is deformed.

These images clearly reveal a rapidly developing cold intrusion (event F2), which appears to grow most strongly after 21 October. During the previous days, 16–20 October, the IFF appears to be oriented in an east–west direction and is relatively inactive. The surface signature of the cold intrusion (Fig. 4b) is much sharper (more crescent shaped) than seen in the lower resolution validating hydrographic survey (Fig. 3b). The cold intrusion is part of a much larger-scale pattern of evolution of the front, which also includes a downstream large-scale eddy feature as well as the upstream northward shift of the front (event F3). The occurrence of the cold tongue intrusion after only 3–4 days exemplifies how rapidly changing and energetic the IFF was during the time of our measurements.

3) SURFACE DRIFTERS

Near-surface drifter (drogued to 15-m depth) observations also are available as additional validation elements for our study (Poulain and Warn-Varnas 1993). During the initialization survey, the velocities computed from the 6-hour interpolated drifter positions provide a good estimate of the magnitude of the IFF current velocity, which helps to constrain the choice of level of no motion (e.g., see section 5b) and substantiate the synopticity of the initial conditions (e.g., see Fig. 8a) and the presence of the cold eddy south of the front. However, away from the strong currents, the drifters do not necessarily corroborate the geostrophic currents, since the drifter velocities include other effects such as Ekman currents, inertial oscillations, tides, etc. Thus, for forecast validation, the velocities computed from drifter tracks can be used only in regions of strong geostrophic currents. Since these regions cannot be identified unambiguously, the drifters can only provide qualitative information on the forecasted surface flows.

c. Caveats

Very poor weather conditions precluded the more extensive and rapid hydrographic surveys that had been originally planned for this cruise. Since the initialization survey required 5.5 days to complete, we must address the question of whether the survey is sufficiently synoptic to be treated so in QG forecasts. It appears that, at least in the western half of the model domain (for 19–22 Oct), the initialization survey (e.g., Fig. 3a) indeed captures a synoptic state as corroborated by supplementary drifter observations (see Fig. 8a) and available satellite SST images (Fig. 4). Little change is observed in the eastern part of the domain during the 1–2 days (23–25 Oct) between the initial and validation surveys.

The nonsynopticity of the initial conditions can be a particularly acute problem insofar as upstream variability affects downstream mesoscale evolution. However, it appears that the cold tongue (F2), which is the most interesting feature of our dataset, develops nearly in place (possibly locked to the large-scale topographic feature over which it grows). The satellite SST images, furthermore, support the notion that the western half of the hydrographic survey adequately represents a rather placid initial state that existed before the cold tongue commenced growth after 21 October. Thus, since the western half of the initial state is relatively synoptic (for that particular time interval) and since the developing cold tongue does not propagate strongly downstream, the initial conditions do seem to be sufficiently synoptic to be treated as such in this study. Note that we also attempt to account for nonsynopticity by using a very simple data assimilation procedure, as described in section 5e. Much more sophisticated techniques exist for determining optimal initial conditions from nonsynoptic data for forecasting applications, such as the generalized inverse method of Bennett and Thorburn (1992) and Bennett et al. (1993).

The qualitative three-feature validation technique is also a serious deficiency of our study, but the unfortunate weather conditions left us with this limited dataset. One could compute anomaly correlation coefficient and rms error statistics between forecast and observed fields along the validation track, but so little data would be involved that the numbers would be of marginal interest. The forecasting component of this study, at the very least, can yield a best QG model that can eventually be tested for quantitative skill in future cruises.

4. Forecast studies: real time

During the October 1992 cruise, as data became available, various forecasts were made using several different forecasting models, among them the QG model herein discussed and an analogously initialized primitive equation model. The results of this shipboard primitive equation forecasting experience will be discussed elsewhere. Here we desire to mention only a few key points from the shipboard QG forecasting study.

TABLE 1. Shipboard QG forecasts [600-m level of no motion, OAP = (60, 40, 0.3)].

Case	Features
SB6-f	Basic flat bottom case
SB6-t	Full topography
SB6-pt	0.8 × topography
SB6-s	Shapiro filter = (4, 2, 2)
SB6-int7	Hindcast; flat bottom; interpolated boundary conditions to day 7

The QG shipboard forecasts (Table 1) all used a 600-m level of no motion. Our choice of objective analysis parameters, OAP = (60, 40, 0.3), while onboard ship resulted in a rather smooth rendering of the IFF (Fig. 5a). The resultant QG current fields were therefore somewhat sluggish and failed to exhibit the very rapid growth of the cold intrusion, although in case SB6-f it did begin to form in the central part of the front by day 6 (Fig. 5b) and moved eastward before breaking off into an eddy by day 8. The potential for improved forecasts was indicated by this result and instigated the extensive OAP study discussed in section 5a.

An interesting result of our shipboard forecasts was that using the full effects of topography (case SB6-t) did not result in a forecast significantly different from the flat bottom QG forecast during the first five or six days, except for some details in the eastern domain. As will be more thoroughly discussed in subsequent sections, the effects of topography did not strongly affect the mechanism involved in developing the surface eddy field.

We carried out several other real-time shipboard QG forecasts and hindcasts. These included a flat bottom run with slightly weaker Shapiro filter damping (SB6-s) and a topographic case with partial strength (SB6-pt). The results did not differ appreciably from the prototype flat bottom case (SB6-f) during the first week or so of the predictions.

We tested the effect of changing western boundary conditions in a hindcast (SB6-int7) at sea that used some information measured during the validation track. The western boundary condition was interpolated from day 0 (initialization survey) to day 7 (validation track) in a hindcast; only the boundary condition has information from the validation track. The main effect is in the vicinity of the western boundary, where the IFF front is shifted northward and broadened, as observed. In the region of the developing cold tongue, the inflow boundary condition has little effect during the initial week due to the cold tongue developing too late and farther downstream than observed. Thus, the guiding influence of the western boundary specification is manifest in this case, although the overly smooth objective analysis is still retarding the developing instability. We therefore proceed with a discussion of some of our sensitivity studies of postcruise forecasts which use initialization information that would nevertheless have been available onboard ship.

5. Forecast studies: postcruise

We have carried out an extensive set of postcruise forecast and hindcast studies. To facilitate discussion of the important effects of these experiments, we have grouped them into various categories in a descriptive fashion. Our goal is to uncover the important features of initialization or of the forecast model itself, which need to be included to yield the best dynamical ocean
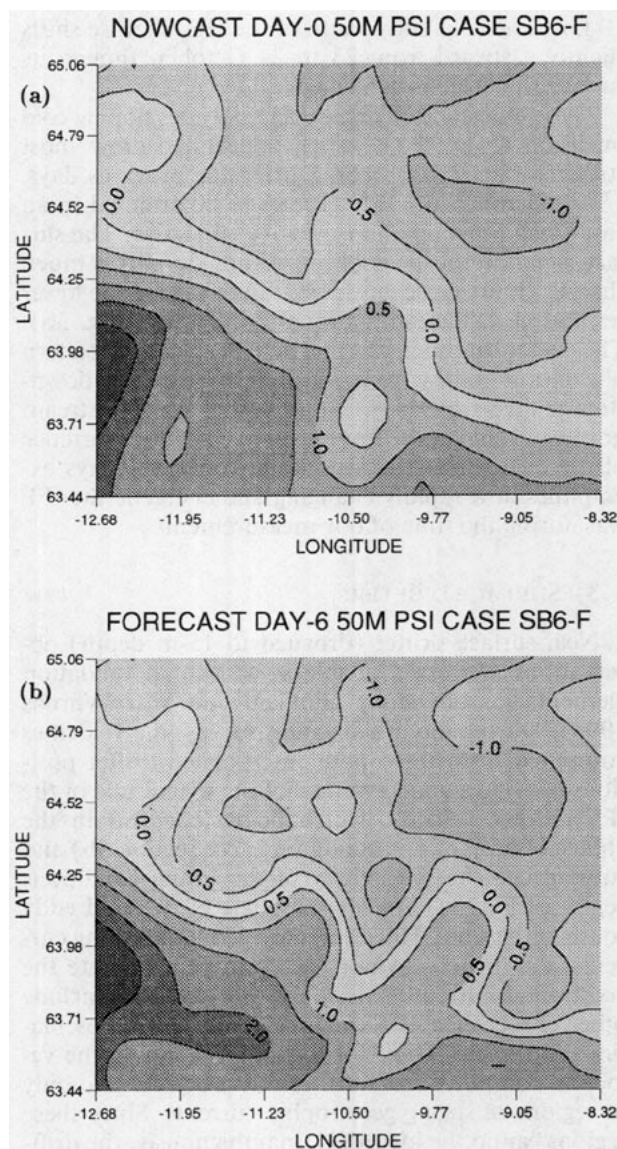

FIG. 5. Case SB6-F (a) initial condition and (b) day 6 forecast of 50-m nondimensional streamfunction (CI = 0.5; multiply by 4500 to redimensionalize to m^2 s^{-1}). This flat-bottom QG forecast was obtained onboard in real time during the Oct. 92 cruise.

forecast possible, given the simplicity of the QG model and the limited set of data we have available for this study. Once this has been accomplished, we can investigate the physical mechanisms leading to the evolution of the IFF field.

a. Objective analysis parameter variations

We ran a series of forecasts with the 600-m level of no motion using differing choices of OAP. The range of OAP (Table 2) results in relatively smoothed versions of the initial field to rather sharp representations of the front. As will be shown, the effect of the initial

TABLE 2. Objective analysis parameters variations forecast series (600-m level of no motion, flat bottom).

Case	Comments	OAP
OA6-1	Cold tongue develops more quickly than SB6-f; flow from NW advects jet S by day 7	(50, 30, 0.1)
OA6-2	Flow from NW impacts jet by day 4	(40, 25, 0.1)
OA6-3	Jet interacts much too strongly with NW flow by day 4	(30, 20, 0.1)
OA6-4	Similar to OA6-3 until day 6	(30, 20, 0.3)
OA6-5	Jet still interacts too strongly with NW flow by day 4	(25, 15, 0.3)
OA6-6	Cold tongue develops by day 4 but downstream and weak; Flow from NW corrupts jet by day 6	(60, 20, 0.1)
OA6-7	Cold tongue better developed than OA6-6; flow from NW corrupts jet by day 7	(60, 10, 0.1)

boundary condition in the western part of the domain is very strong. Depending on how the initial streamfunction field intersects the boundary, inflow or outflow regions are set up in the model domain and these flows can substantially affect the developing interior flows.

Cases OA6-1, OA6-2, and OA6-3 use increasingly shorter length scales in their sets of OAP than were used on the cruise. In both cases OA6-1 and OA6-2, the cold tongue intrusion begins to develop by day 4 of the forecasts. However, the developing cold tongue is disturbed by flow from the northwestern corner of the basin, established by the initial boundary condition there, which tends to collide with the IFF current and deflect it southwards in the western half of the domain. This effect of the inflow condition in the northwest becomes even more apparent in case OA6-3, which via a strong interaction of the IFF current and this NW inflow results in a substantial northward loop of the IFF current at the western boundary that merges with the southeastward flow from the NW corner (Fig. 6). Clearly, the IFF current is much too vigorously unstable in this configuration. Even a minor change in the OAP (case OA6-4) results in some sizable changes in the details of the flow by day 7. We anticipated that if the flow impinging on the IFF from the NW corner of the basins could be muted by a suitable choice of OAP, then the developing instability in the IFF might be sufficiently energetic to produce the rapid development of the cold tongue, as was observed.

Decreasing the exponential decay scale (OA6-5) does not result in a significantly reduced flow from the NW to alleviate the problem with the inflow boundary condition. By extending the length scale of the zero crossing of the OAP (case OA6-6), the streamfunction in the NW corner of the basin has a much smoother structure and results in a weaker flow into the interior basin. The forecast for this case indeed has a nicely developed cold tongue by day 4, though it is still weaker than observed and too far downstream. A further reduction

in the e-folding scale of the correlation function (case OA6-7) results in what we consider to be the best forecast of this series (Fig. 7). Part of the improvement lies in the fact that the OAP for case OA6-7 resolves a "kink" (at 64.1°N, 11°W) in the initial IFF current that seeds the development of the cold tongue. But the key point is the weaker impact of the flow from the northwest induced by the initialization of the boundary conditions.

Our results of this subsection show that it is imperative in this domain to produce relatively smooth boundary conditions away from the IFF inflow in the initial objective analysis; significant structure in the boundary condition can result in inflow/outflow patterns that can potentially interact strongly with the in-
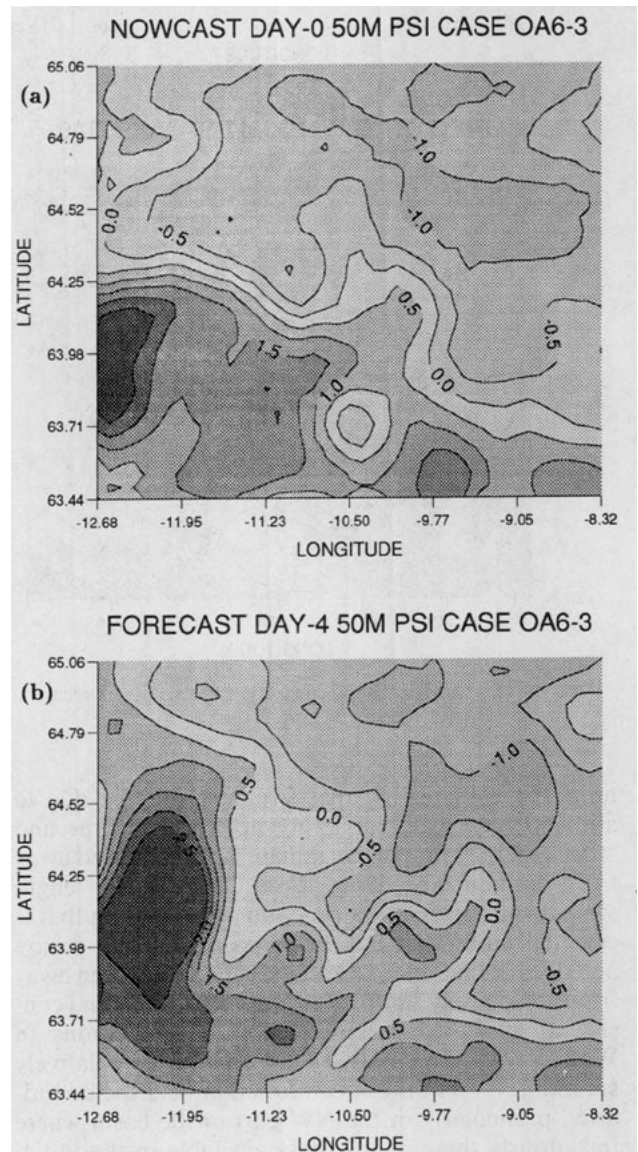

FIG. 6. Case OA6-3 (a) initial condition and (b) day-4 forecast. Otherwise as in Fig. 5.

NOWCAST DAY-0 50M PSI CASE OA6-7
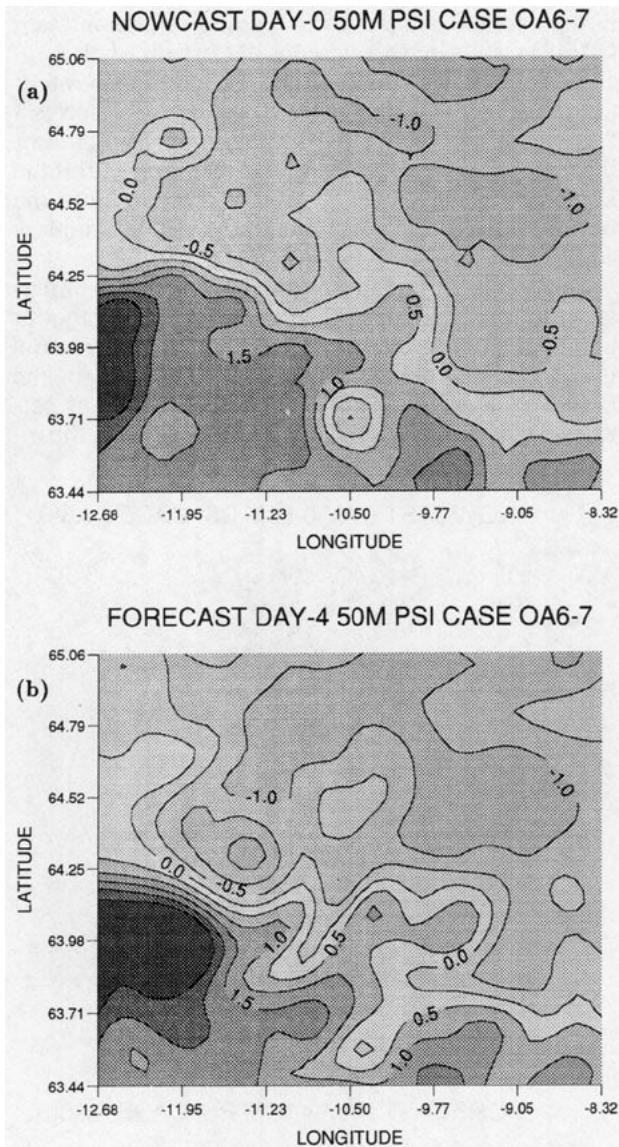

FORECAST DAY-4 50M PSI CASE OA6-7

FIG. 7. Case OA6-7 (a) initial condition and (b) day-4 forecast. Otherwise as in Fig. 5.

terior flow. In reality, that structure may be due to ambient mesoscale variability not fixed in time and space and may propagate, radiate, or be advected away from domain boundaries. Case OA6-7 has a length scale for the correlation function zero crossing that is essentially infinite so that the correlation quickly decays and does not produce false eddies of opposite sign away from the densely sampled region of the domain (consistent with the objective mapping conclusions of Warn-Varnas et al. 1993). This results in the relatively smooth roll-off of the streamfunction near the boundaries, particularly in the NW part of the basin where fortuitously there is little data available in the initial survey. Keeping these results in mind, we explore next the consequences of changing the level of no motion.

b. Choice of the level of no motion

Changing the level of no motion to a shallower level in the QG model results in weakened currents near the surface. Although we tested several different levels of no motion in forecasts, it became clear that 400 m was the best choice, particularly when comparing the diagnosed surface geostrophic currents with estimates of surface currents from the drifter datasets (Fig. 8a). Peak speeds in the IFF current were typically observed to be 60 cm s^{-1} by the drifters, very much like the peak speeds seen in the 400-m objective analyses series listed in Table 3.

Comparing case LV4-1 with OA6-7 reveals that the cold tongue develops as strongly for the 400-m level

NOWCAST DAY-0 LV4-1, DRIFT VELS 21,23OCT

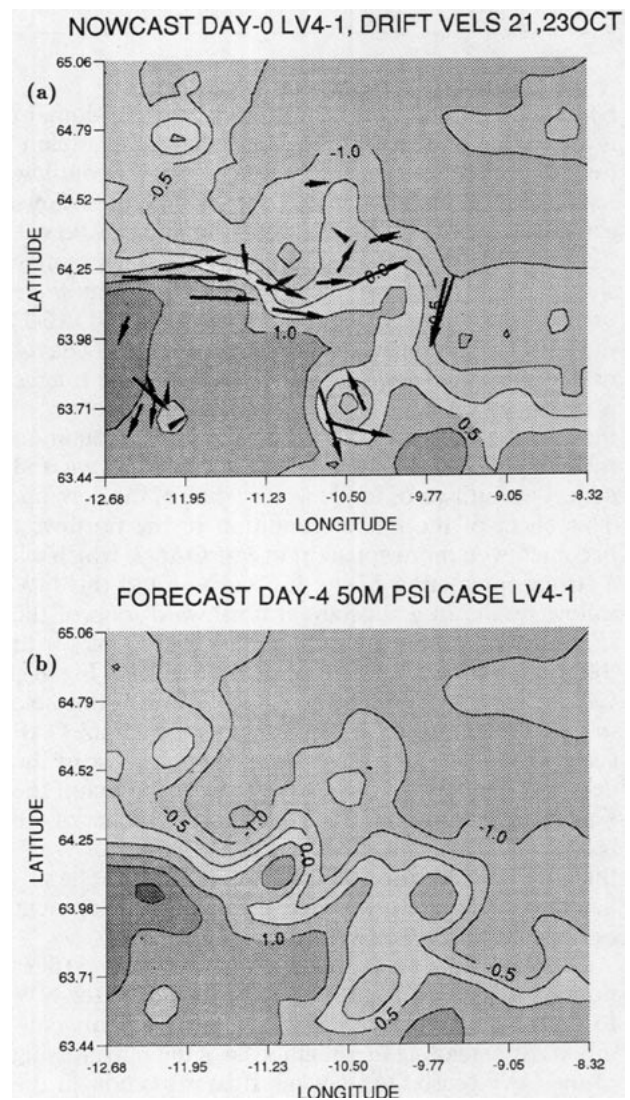FORECAST DAY-4 50M PSI CASE LV4-1

FIG. 8. Case LV4-1 (a) initial condition and (b) day-4 forecast. Drifter displacement from 21 Oct. and 23 Oct. are superposed in (a). Arrow length is the distance traveled during the 24-h day (so that an arrow with length equal to one tick mark in latitude corresponds to a velocity estimate of 35 cm s^{-1}). Otherwise as in Fig. 5.

TABLE 3. 400-m level of no motion variations forecast series.

Case	Comments	OAP/Initial deep layer
LV4-1	Cold tongue well developed, but weaker than observed	(60, 10, 0.1)/zero
LV4-2	Cold tongue develops late (day 7)	(60, 20, 0.1)/zero
LV4T	Topo; jet shifts S by day 7; weak cold tongue	(60, 10, 0.1)/zero
LV4A	Cold tongue develops by day 4 Strong breakdown of jet by day 7	(60, 10, 0.1)/active
LV4AT	Topo; cold tongue pinches off by day 4 jet stronger compared to LV4A	(60, 10, 0.1)/active

of no motion case (Fig. 8b) but that by day 7 case LV4-1 has a much more realistic flow. There is little evidence for strong flow from the NW advecting the frontal current southward, and the cold tongue has developed well to the south of the IFF without much eastward propagation as the observations suggest. Furthermore, the cold eddy that existed south of the IFF remains persistent in shape and exhibits weak eastward migration as seen in the satellite SST images.

Since case LV4-1 represents nearly the best case of our entire analysis, we now outline what improvements are sought. The cold tongue needs to be increased in amplitude and in southward penetration, as well as to develop substantially by the third day of the forecast rather than the fourth day. Furthermore, the cold tongue tends to develop slightly farther downstream than observed; this tendency may be alleviated by either more rapid development or by suppressing the effects of horizontal advection by the IFF current. We now explore other scenarios in the 400-m level of no motion situation.

Increasing the e-folding length scale (case LV4-2) weakens the surface currents further and results in the cold tongue developing even later than in case LV4-1. Shortening the e-folding scale results in little change in the initial conditions, since the measurements were taken roughly 10 km apart. If the full effect of topography is included in the forecast (LV4T), by day 4 the cold tongue is slightly weakened and by day 7 the entire IFF has been shifted southward by 50 km.

The previous three cases used a 400-m level of no motion, but with the 600-m QG level also set equal to zero as the initial condition. We explored the effect of "activating" the initial 600-m QG layer in cases LV4A and LV4AT; that is, instead of setting the QG streamfunction to zero at 600 m, the dynamic height relative to 400 m is computed for that layer. In case LV4A, the cold tongue develops slightly farther upstream, an improvement over case LV4-1, although the southward extension of the tongue is slightly weaker (Fig. 9). By day 5 the cold tongue pinches off into a cold eddy and

further evolution of the flow field is rather complicated, resembling a field of eddies rather than a zonal current. By day 7 the flow near the western boundary is displaced northward (verification event F3), unlike LV4-1. All in all the results appear to be slightly better for LV4A than LV4-1. Adding the full effects of topography (case LV4AT) results in the cold tongue pinching off by day 4 and the jet strengthening via the occurrence of a dipole-like structure on either side of the IFF current from day 4 through day 7. The basic features seen in the first few days of the forecasts are similar to the flat bottom analog.

We also tested a few cases (not listed) in which we added or subtracted small fractions of the surface streamfunction to all the layers as a measure of the "barotropic mode" in the initial conditions. The results did not seem to improve the forecasts for either the 600- or 400-m level of no motion scenarios, so we do not discuss these results any further.

c. Idealized IFF jets

We have shown that the boundary conditions, which are normally persisted throughout the forecast, have a strong effect on the interior flow evolution. We therefore explored the effects of smoothing the boundary conditions by eliminating the ambient mesoscale variability surrounding the IFF current. These runs are meant to elucidate the importance of instabilities in the IFF current acting in isolation from the surrounding mesoscale and boundary inflow conditions resulting from the initial objective analysis.

To create a model IFF jet, we computed the average streamfunction for all values exceeding chosen streamfunction values on either side of the observed jet. For example, in the top layer for case JM4-1, all grid points
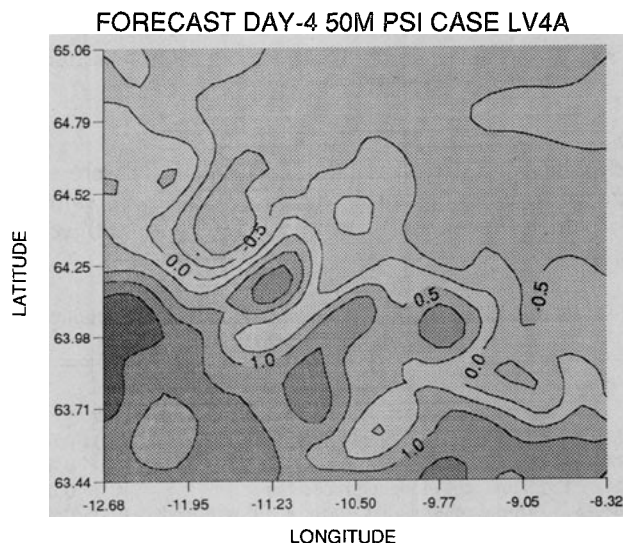
FORECAST DAY-4 50M PSI CASE LV4A

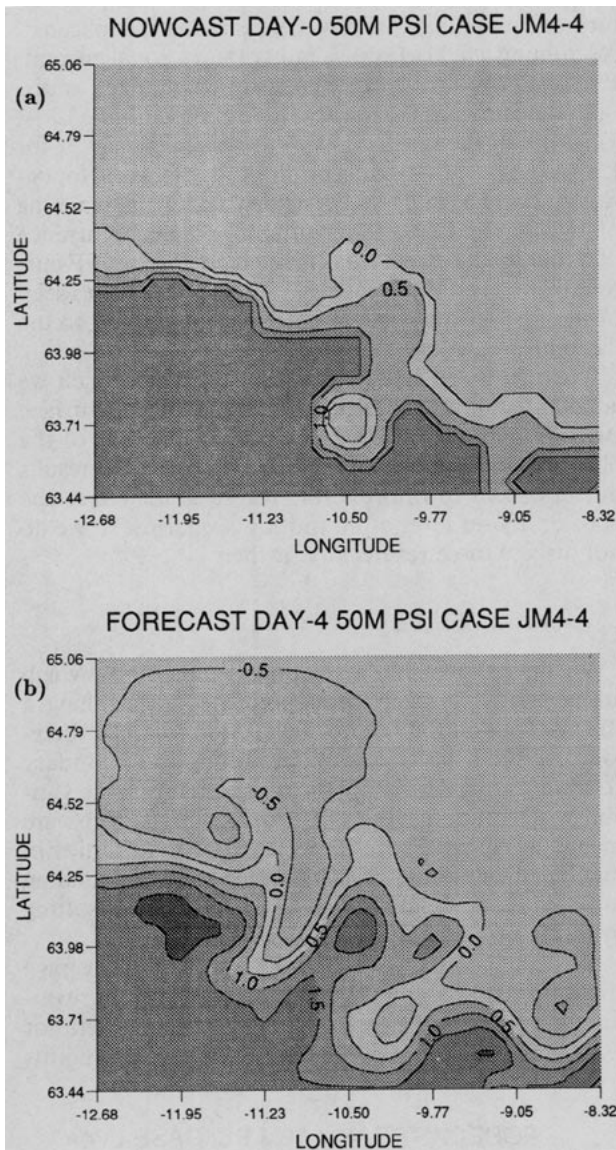FIG. 9. Case LV4A day-4 forecast. Otherwise as in Fig. 5.

FIG. 10. Case JM4-4 (a) initial condition and (b) day-4 forecast. Otherwise as in Fig. 5.

for which the streamfunction exceeded 0.04 were averaged together (resulting mean = 0.085). All values for which the streamfunction was less than 0.00 were

TABLE 4. Model IFF jets forecast series [400-m level of no motion/ OAP = (60, 10, 0.1)].

Case	Comments	$\pm\psi_{crit}$
JM4-1	IFF jet rapidly breaks down into eddies	(0.04/0.00)
JM4-2	Cold tongue develops	(0.06/0.00)
JM4-2T	Topo; cold tongue pinches off	(0.06/0.00)
JM4-3	Initial small eddies north of IFF removed; similar to JM4-2	(0.06/0.00)
JM4-4	Larger amplitude cold tongue	(0.06/0.01)

TABLE 5. Changes in boundary conditions forecast/hindcast series [OAP = (60, 10, 0.1)].

Case	Comments	Level of no motion/initial deep layer
BC4X	As in LV4A but pseudodata in NW domain	400 m/active
BC4XI	As in BC4X but interpolate to B.C. by day 7	400 m/active
BC4I	As in LV4A but interpolate to B.C. by day 7	400 m/zero
BC4XIJ	Interpolate to model jet 4 by day 7	400 m/active
BC6D-1	West boundary moved in by 20 km	600 m/na
BC6D-2	West boundary moved in by 30 km	600 m/na

also averaged together (mean = −0.030). Then, those values which contributed to the average were set equal to the average value. This results in a jet (Fig. 10a) that looks very much like the original objective analysis, but with most of the field away from the jet (including the boundaries) equal to one of two constant values. A similar procedure was done for all the remaining layers. The other cases in this series use differing choices for the critical streamfunction values, and/or remove minor eddies that remained in the "flat" streamfunction regions. The cold eddy that is initially south of the IFF in the initial objective analysis is always included in these runs. All the runs use a 400-m level of no motion and an "active" 600-m initial condition as in case LV4A. Table 4 lists the critical ψ values used in the top two layers; the middle layers always use ψ_{crit} = (0.03, 0.00), and the bottom layer uses ψ_{crit} = (0.015, 0.005).

For case JM4-1, the chosen critical values of ψ result in a jet that is too weak to be persistent. The result is that the jet rapidly breaks down into a series of three eddies, unlike the observations. For a broader initial jet, as in case JM4-2, the model jet develops a very nice cold tongue, although it is still somewhat weaker and develops farther downstream than observed. When topography is included (JM4T-2) the cold tongue pinches off to form a ring by day 4, unlike the observations but similar to LV4AT, and occurs downstream of the actual cold tongue. Case JM4-3 is identical to JM4-2 except all points north of 64.55°N are included in the local average of points, thereby eliminating two

TABLE 6. Building domain forecast series [400-m level of no motion; OAP = (60, 10, 0.1); deep layer active].

Case	Comments
BD4X	Cold tongue poorly developed
BD4XT	Topo; strong IFF current advects cold tongue downstream

NOWCAST DAY-0 50M PSI CASE BC4X

(a)

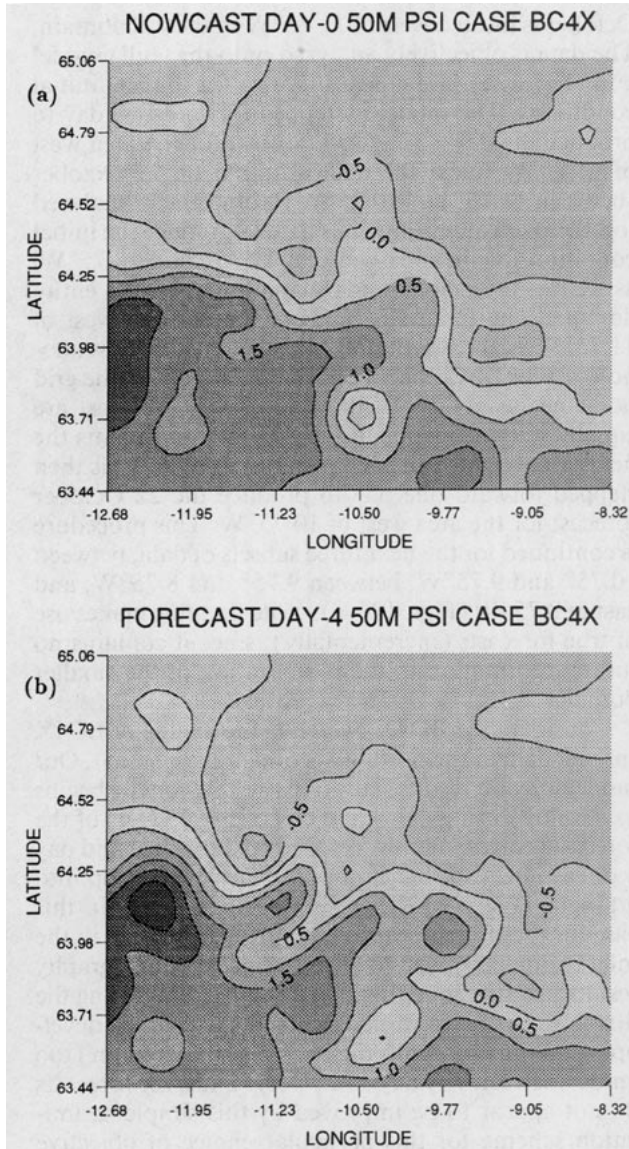## FORECAST DAY-4 50M PSI CASE BC4X

(b)

FIG. 11. Case BC4X (a) initial condition and (b) day-4 forecast. Otherwise as in Fig. 5.

small eddies, which occur as blips on the flat region. The result is essentially the same as JM4-2. Case JM4-4 uses critical values that result in a slightly narrower jet. The result (Fig. 10b) shows a stronger cold tongue developing, though again it appears to be advected downstream compared to observations.

These results show that the development of the cold tongue is controlled by processes intrinsic to the IFF current itself. The effects of the boundary conditions away from the frontal inflow and the effects of the surrounding mesoscale have been removed, yielding a "pure" growth of the jet. Topography has little importance in the first few days of the pure growth of the cold tongue in this set of experiments. These results are consistent with the primitive equation modeling

results of Maskell et al. (1992), who examined the growth of perturbations in initially zonal jets over various topographies including the effects of nearby eddies.

d. Boundary condition variations

To further understand how the boundary conditions affect the QG forecasts, we ran several sets of differing types of experiments. The first test was an attempt to encourage a smoother inflow in the NW corner of the domain by creating extra data points to "fill in" the unmeasured line north of 64.5°N, along 12.5°W. These pseudodata points are simply reproductions of the analogous measurements[3] to the east, along 12°W. The resulting objective analyses with the pseudodata are, of course, only affected in the region near the false data and they indeed result in a smoother boundary condition in the NW corner of the basin (Fig. 11a). The forecasting results of case BC4X (Fig. 11b) are that the cold tongue is reduced in amplitude but also that the IFF current tends to arch northward more so than in case LV4A near the inflow at the western boundary. Furthermore, by day 7 the frontal current is still intact in case BC4X rather than having broken down into a field of eddies. These are a mixture of slight improvements and degradations over case LV4A.

We also ran a set of hindcasts in which the boundary conditions were linearly interpolated from those of the initialization survey (day 0) to those of the verification track (day 7). The day-7 boundary conditions were

[3] It was at this point that we noticed the inadvertent inclusion of a bad XCTD at (64.75°N, 12°W) whose salinity offset, when averaged with a contemporaneous CTD, resulted in a small dome of dynamic height; recomputations of a selection of previous cases showed little differences due to the presence of this small erroneous warm eddy.
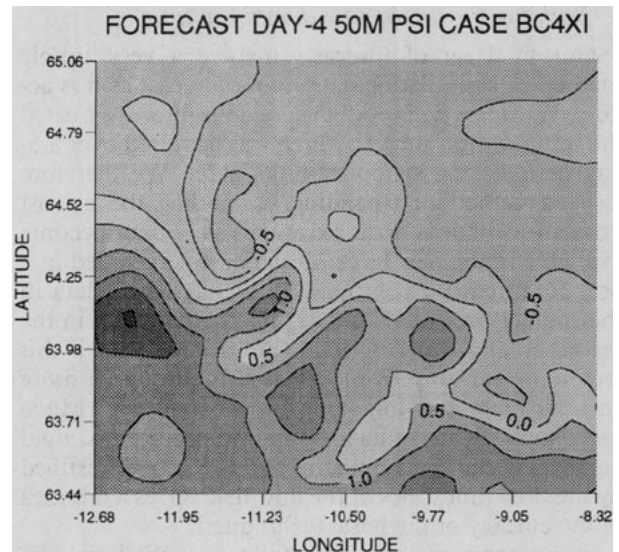
FORECAST DAY-4 50M PSI CASE BC4XI

FIG. 12. Case BC4XI day-4 hindcast. Otherwise as in Fig. 5.

obtained from the objective analysis that included all data of the verification track and all data of the initialization survey except those stations south of 64.55°N and west of 11.75°W, that is, the area around the western boundary where the validation track exists. These experiments help us to identify the effects of the changing inflow conditions on the developing interior field.

Case BC4XI, for instance, results in two improvements over the forecasts (Fig. 12). First, the IFF current near the inflow is broader (as observed) than the persistent boundary condition case BC4X. Also, the cold tongue that develops is now stronger and pinches off by day 5 of the hindcast. However, for case BC4I, which does not include the pseudodata in the NW corner of the basin, the flow is degraded by day 7 due to a strong flow from the NW interacting strongly with the developing cold tongue.

In case BC4XIJ (a true forecast), we used the model jet case JM4-4 initial conditions as the day-7 boundary conditions to which we interpolate the (true) forecast using the same parameters as case BC4X. However, compared to case BC4X, this did not result in any significant differences in the flow field away from the immediate vicinity of the western boundary.

We also tested the effect of improving the accuracy of specifying the inflow boundary condition by reducing the size of the domain by moving the western boundary of the domain eastward by 20 km (case BC6D-1) and 30 km (case BC6D-2), each with a 600-m level of no motion. In both cases, the cold tongue grows excessively to the extent that by day 7 it had absorbed the cold eddy south of the IFF current. Apparently, the narrow IFF current held fixed as the western boundary condition in these two cases results in a too strong advective effect and, hence, a too energetic instability.

e. Building the forecasting domain in time

Our final set of forecasts involve a very simple method of assimilating data into a forecast as it is acquired during a cruise. All the previous forecasts treated the initialization survey, which was acquired over a 5-day period, as a synoptic initial state. We therefore tested a method for expanding, or building, the forecast domain as data is acquired. Once new data become available in the new larger domain, it is included in a pseudonowcast, a combination of forecasted data in the smaller previous domain plus the new data in the incrementally larger domain. We desire to see if this technique can improve the forecasts through a more accurate representation of the initial conditions. (Much more sophisticated data assimilation procedures could be devised, but the simplicity of this method, justified by the slow timescales of the flow field, gives a fair idea of the efficacy of the basic technique.)

Our specific exercise is the following. We break the data up into five subsets. The data acquired on 19–20

October is located west of 11.75°W in the full domain. The data is objectively analyzed onto the (full) model grid (Fig. 13a) and constitutes day 0 (20 Oct) initial conditions. The model is stepped forward one day to produce the day 1 (21 Oct) forecast for the area west of 11.75°W. Next the data acquired on 21 October (between 11.75° and 10.75°W) is objectively analyzed together with all the previous data to produce the initial condition for the area between 11.75° and 10.75°W, as well as the new boundary condition for the entire domain. The forecasted data in the domain west of 11.75°W is then smoothly merged into this pseudo-nowcast for 21 October (Fig. 13b); namely, at the grid point nearest 11.75°W the forecast and nowcast are equally weighted while at the adjacent grid points the fields are weighted in a 3 to 1 ratio. The model is then stepped forward one day to produce the 22 October forecast for the area west of 10.75°W. This procedure is continued for the next three subsets of data, between 10.75° and 9.75°W, between 9.75° and 8.75°W, and east of 8.75°W (Figs. 13c–e). Note that this makes use of true forecasts (incrementally), since it contains no future information in the initialization of the smaller domains.

Consider case BD4X, which is the analog of BC4X (pseudodata in the northwest corner of the basin). Our model forecast results show that the cold tongue begins to develop during day 4 and day 5 (24–25 Oct) of the forecast (corresponding, respectively, to day 3 and day 4 of case BC4X), but it does not clearly develop into a tongue (Fig. 13f). There is a clear tendency in this case for the IFF current to be shifted northward in the inlet region, as observed. The inclusion of topography results in a strengthening of the IFF current during the first few days. This stronger current advects the developing cold tongue into the center of the domain (too far downstream) by day 5 (25 Oct). Thus, the forecasts do not appear to be improved by this simple assimilation scheme for this particular choice of objective analysis parameters (which were selected based on their forecasting performance when treating the initially conditions synoptically). Although we tried a few other scenarios (e.g., with differing objective analysis parameters) that resulted in only small differences from the above results, we only superficially explored this assimilation framework. Within the subset of model frameworks that we herein examined, allowing the nonsynoptic initial conditions to develop together resulted in better forecasts.

f. Comparison with surface drifters

The near-surface drifter measurements, though influenced by other processes than simply geostrophic currents, provide another view of the validity of the forecasts. We focus only on the development of the cold tongue (forecast day 3 through day 6) and examine one of the best forecasts, Case BC4X. Figure 14 shows
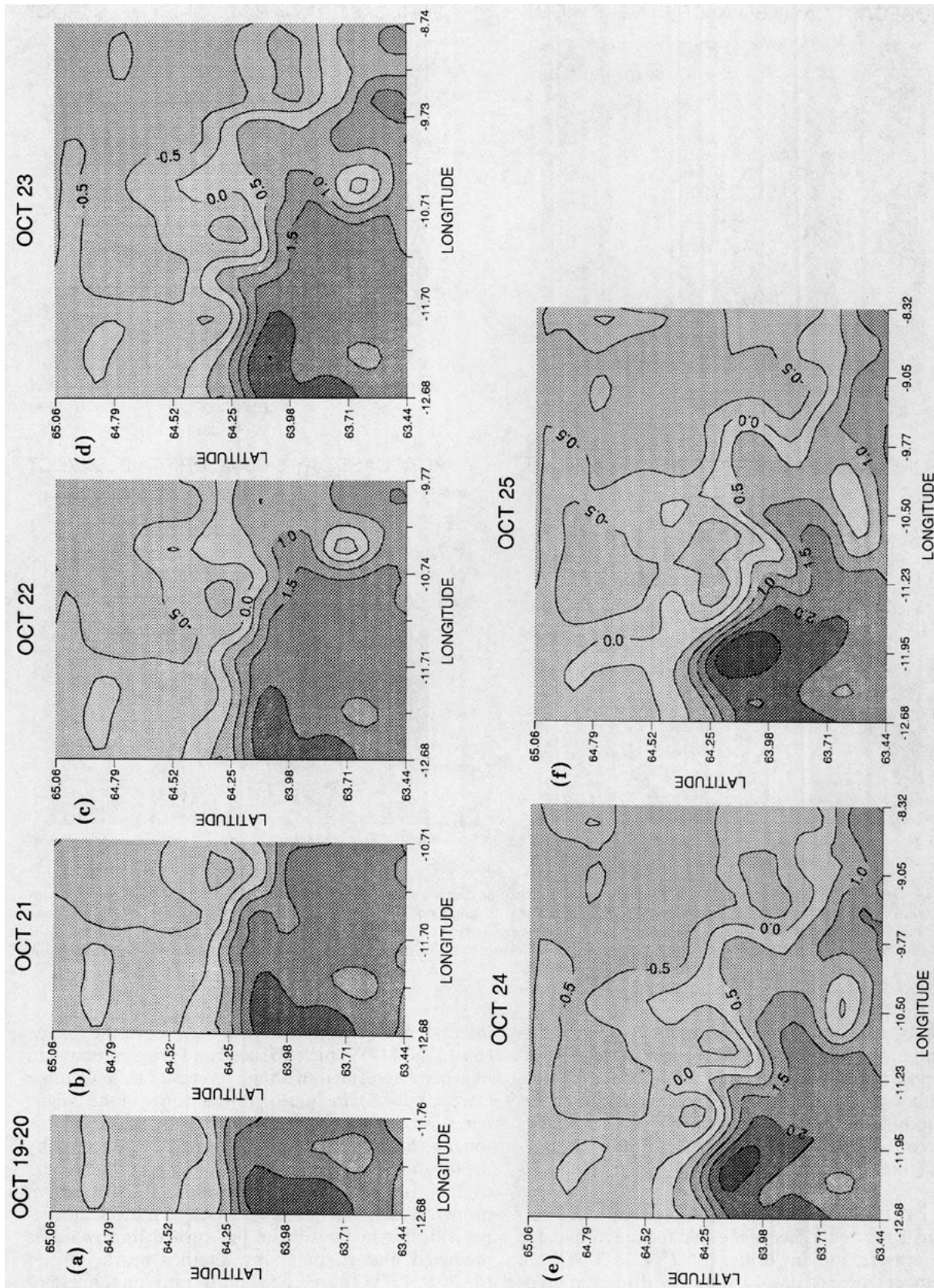
MILLER ET AL.

FIG. 13. Case BD4X (a) 19–20 Oct. nowcast, (b) 21 Oct. nowcast/forecast, (c) 22 Oct. nowcast/forecast, (d) 23 Oct. nowcast/forecast, (e) 24 Oct. nowcast/forecast, and (f) 25 Oct. forecast. Otherwise as in Fig. 5. Only that part of the domain in which data exists is shown. As data is acquired during the initial cruise track, forecasts from the previous domain are combined with the new data in the larger domain.
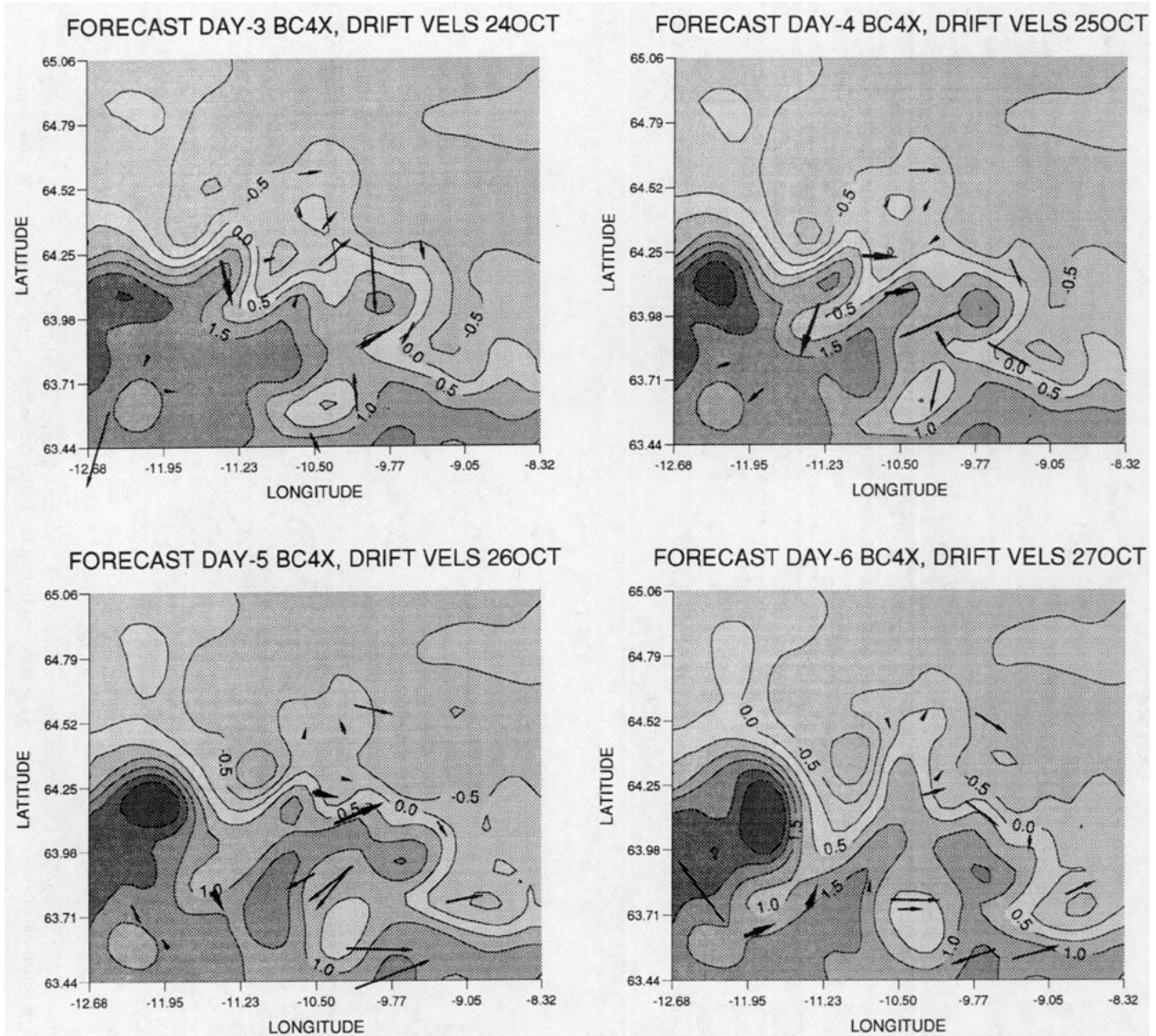
FORECAST DAY-3 BC4X, DRIFT VELS 24OCT

FORECAST DAY-4 BC4X, DRIFT VELS 25OCT

FORECAST DAY-5 BC4X, DRIFT VELS 26OCT

FORECAST DAY-6 BC4X, DRIFT VELS 27OCT

FIG. 14. Case BC4X day 3 through day 6 forecasts with 1-day drifter displacements from 24 Oct. through 27 Oct. superposed. Arrow length is the distance traveled during the 24-h day (so that an arrow with length equal to one tick mark in latitude corresponds to a velocity estimate of 35 cm s^{-1}). Only the drifters in the vicinity of the developing cold tongue (thick arrows) correspond to the proper time of the forecast (due to the 5-day time interval required to obtain the initial survey). The other drifters (thin arrows) are shown only for potential interest.

all the 1-day drifter trajectory segments (plotted as vectors) in the domain for 24 through 27 October superimposed on the corresponding forecast days. Note that although all the drifters are shown, only the region surrounding the developing cold tongue corresponds to the correct forecast time; the other drifter displacements (thin arrows) are shown only for potential interest.

On 24 October (forecast day 3) the southward current predicted on the face of the cold tongue is validated by a southward moving drifter (64.2°N, 11.3°W). On 25 October (forecast day 4), the same drifter proceeds farther south of 64°N, in agreement with the model

forecast. Also, two drifters near the root of the tongue (64.15°N, 11°W) pick up speed and progress eastward in general agreement with the forecast. On 26 October (forecast day 5), the southernmost drifter in the tongue has slowed and turned eastward near the tip of the tongue (63.8°N, 11.5°W), as would be expected by the forecasted current field. The other two drifters (near 64.2°N, 10.5°W) continue eastward in the IFF current proper. By 27 October (forecast day 6), the southernmost drifter in the tongue has turned northward as predicted and is joined by another nearby drifter (63.7°N, 12°W) also headed northwards on the eastern flank of the tongue.

In general, therefore, the surface drifters in the vicinity of the developing cold tongue corroborate the model's predicted surface current field. But we must emphasize that many other processes can contribute to the movement of the surface drifters and that not all the drifters in the model domain behave as would be expected by geostrophic advection (even in the dense initial survey as seen in Fig. 8a).

g. Summary of validations

We have found that the best forecasts validated well against the three events identified in section 3. The key event (F2) is the rapid, intense development of the cold tongue by day 3 or 4 of the forecast, which was indeed seen in some form or another in most of the forecasts. However, in the forecasts the intensity and rapid growth were both underpredicted. Although a weak eastward migration of the entire IFF eddy pattern is seen in the satellite images from 23 to 24 October, the model-generated eastward migration of the IFF eddy pattern is somewhat stronger than observed, as is evident in the direct comparison of forecast day 4 of case BC4X and the hydrocast observations (Fig. 15). The near-surface drifter displacements in the vicinity of the developing cold tongue event further corroborate the model's forecasted near-surface velocity field (Fig. 14). The forecasts clearly show that the current disappearance event (F1) is associated with the formation of the cold tongue (event F2); while the tongue forms, the IFF current shifts its position. Feature F1 validates in most of the forecasts as well, though again a bit farther downstream than observed. The final event (F3), the northward shift of the IFF at the inlet boundary condition by day 6 or 7, tends to occur in the best forecasts as well. This feature, though, is strongly influenced by the persistent boundary condition necessarily employed. The frontal current there must stay attached to the initial boundary condition and therefore cannot broaden as much as in the observations, though it does arch northwards in the best forecasts. The cold eddy, which was initially south of the IFF, is also forecast in many cases to remain relatively persistent in shape and to weakly migrate eastward as seen in the satellite images.

6. Physical processes

We seek to understand what mechanisms control the development of the cold tongue intrusion, which grows over a time interval of 3 to 5 days. Pinardi and Robinson (1986) have developed a procedure of diagnosing the energetics of an evolving QG field, and we adopt this strategy here.

The programs compute, as a function of time, horizontal position, and QG layer, the terms in the QG kinetic and potential energy equation. We have diagnosed several different forecast cases discussed above,
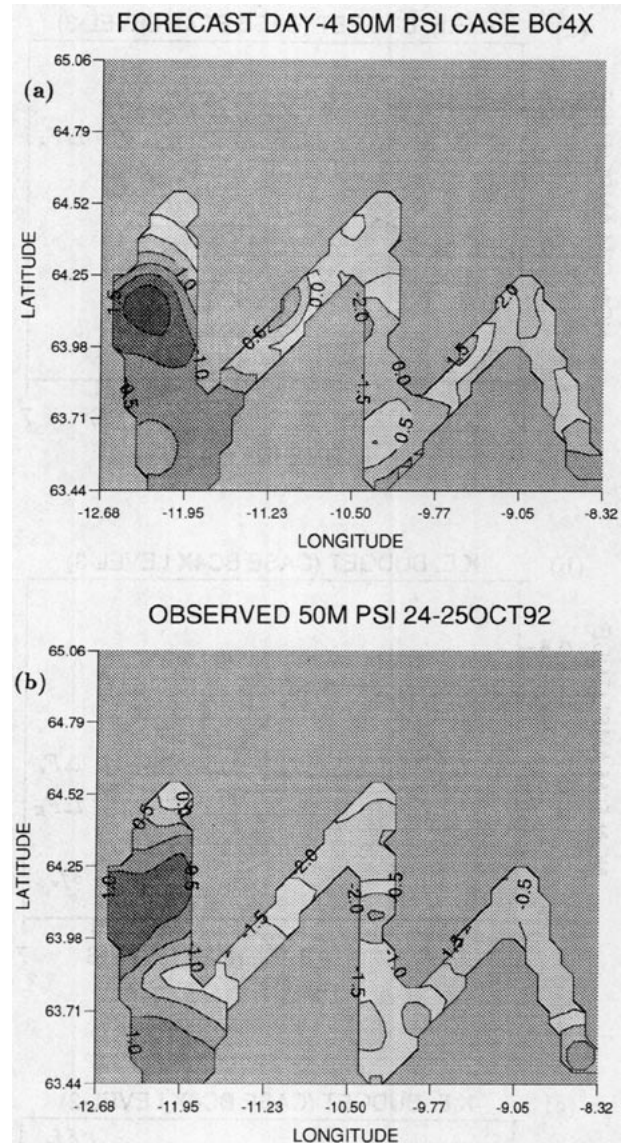

FIG. 15. Direct comparison between 50-m streamfunction (a) forecast for day 4 in Case BC4X with (b) the observations for 24/25 Oct. The area of the observations that should be compared to the day-4 forecast is only in the region surrounding the cold tongue.

but we concentrate here on what we presume to be the most realistic case (BC4X) based on skill of the forecast. We draw upon the set of models considered by Pinardi and Robinson (viz., a baroclinic Rossby wave, the Eady baroclinic instability result, a barotropic instability result, and a OPTIMA-V eddy merger event) for insight into delimiting the mechanisms for variability in the IFF. We seek to determine whether the cold tongue intrusion event (F2) forecast and discussed in the previous sections was caused by baroclinic instability, barotropic instability, or perhaps some other, less obvious mechanism.

The quasigeostrophic kinetic and available gravitational potential energy (KE and AGE) equations in

(a)   A.G.E. BUDGET (CASE BC4X LEVEL-3)

(b)   K.E. BUDGET (CASE BC4X LEVEL-3)

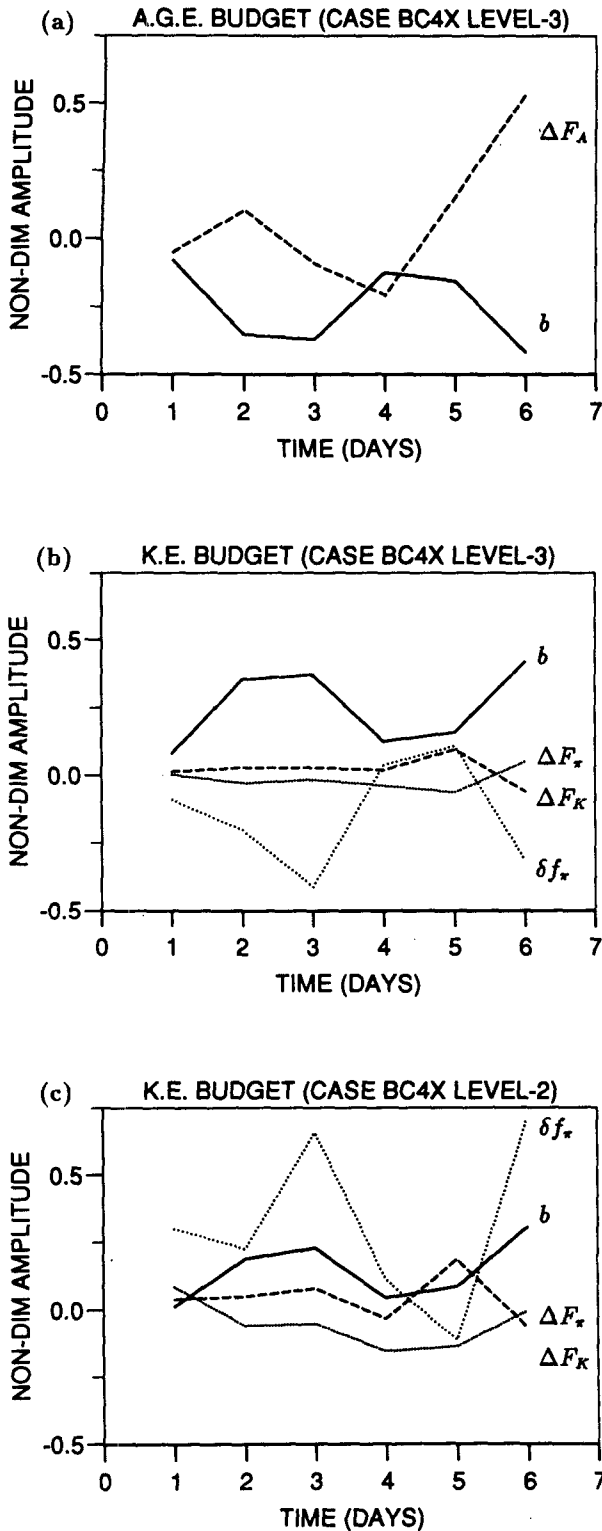**(c)   K.E. BUDGET (CASE BC4X LEVEL-2)**

FIG. 16. Case BC4X terms in the (a) AGE equation at level 3, (b) KE equation at level 3, and (c) KE equation at level 2, averaged over the subdomain of Fig. 1b surrounding the developing cold tongue instability. The symbols for the terms in each equation are defined in Eqs. (1) and (2). The amplitude is nondimensional (following Pinardi and Robinson 1986).

nondimensionalized form are (see Pinardi and Robinson 1986 for full details)

$$\dot{K} = -\alpha\nabla\cdot(\mathbf{u}K)$$

$$- \nabla\cdot(p\mathbf{k}\times\mathbf{u}_t + \alpha p\mathbf{u}\cdot\nabla(\mathbf{k}\times\mathbf{u}) - \beta y p\mathbf{u})$$

$$+ (p\sigma\Gamma^2 p_{zt} + p\alpha\Gamma^2\sigma\mathbf{u}\cdot\nabla p_z)_z + \delta_0 w \qquad (1)$$

$$= \Delta F_K + (\Delta F^t_\pi + \Delta F^\alpha_\pi + \Delta F^\beta_\pi)$$

$$+ (\delta f^{\,t}_\pi + \delta f^{\,\alpha}_\pi) - b \qquad (1a)$$

$$= \Delta F_K + \Delta F_\pi + \delta f_\pi - b \qquad (1b)$$

$$\dot{A} = -\alpha\nabla\cdot(\mathbf{u}A) - \delta_0 w \qquad (2)$$

$$= \Delta F_A + b, \qquad (2a)$$

where the variables in (1), (2) have their usual physical oceanographic meanings and the symbols in (1a), (1b), (2a) correspond to the terms in (1), (2) for ease in subsequent referencing. The nondimensional parameters are $\alpha = t_0 V_0/D$, $\Gamma^2 = f^2_0 D^2/N^2_0 H^2$, $\sigma = N^2_0/N^2(z) = -N^2_0/g(\partial\rho/\partial z)$, and $\beta = \beta_0 t_0 D$, where t_0, D, and H are the characteristic time, depth, and length scales and f_0, β_0, and N_0 are representative values of the Coriolis frequency, its meridional derivative, and the buoyancy frequency.

The symbols representing the terms in (1), (2) are ΔF_K, the horizontal KE advective working rate; ΔF_π, the horizontal pressure working rate, which is further broken up into three terms: ΔF^t_π, that due to acceleration of the geostrophic velocity, ΔF^α_π, that due to advection of the geostrophic velocity, and ΔF^β_π, that due to Coriolis acceleration; δf_π, the vertical pressure working rate, which is further separated up into two terms: $\delta f^{\,t}_\pi$, the vertical pressure energy flux divergence due to time changes in density, and $\delta f^{\,\alpha}_\pi$, the vertical pressure energy flux divergence due to horizontal advection of density; b, the buoyancy working rate; and ΔF_A, the horizontal AGE advective working rate.

Before commencing the energetic analysis of the best forecast, we briefly summarize the basic signatures of baroclinic and barotropic instability according to the idealized model results of Pinardi and Robinson (1986). In their Eady baroclinic instability model (pure vertical shear), buoyancy work is negative definite in middepths of the water column, indicating a transfer of energy from AGE to KE. The source term for the AGE is the energy of the shear flow, arising through ΔF_A. Besides the forcing through buoyancy coupling at middepths, the KE equation is driven near the surface through vertical exchange processes, δf_π in the baroclinically unstable case. The term δf_π drains the KE at middepth and drives the KE at the vertical boundaries. In the barotropic instability model (pure horizontal shear) of Pinardi and Robinson, the AGE equation is inconsequential. The dominant source term in the KE equation is ΔF_κ, corresponding to a Reynolds stress effect drawing energy from the mean shear. We
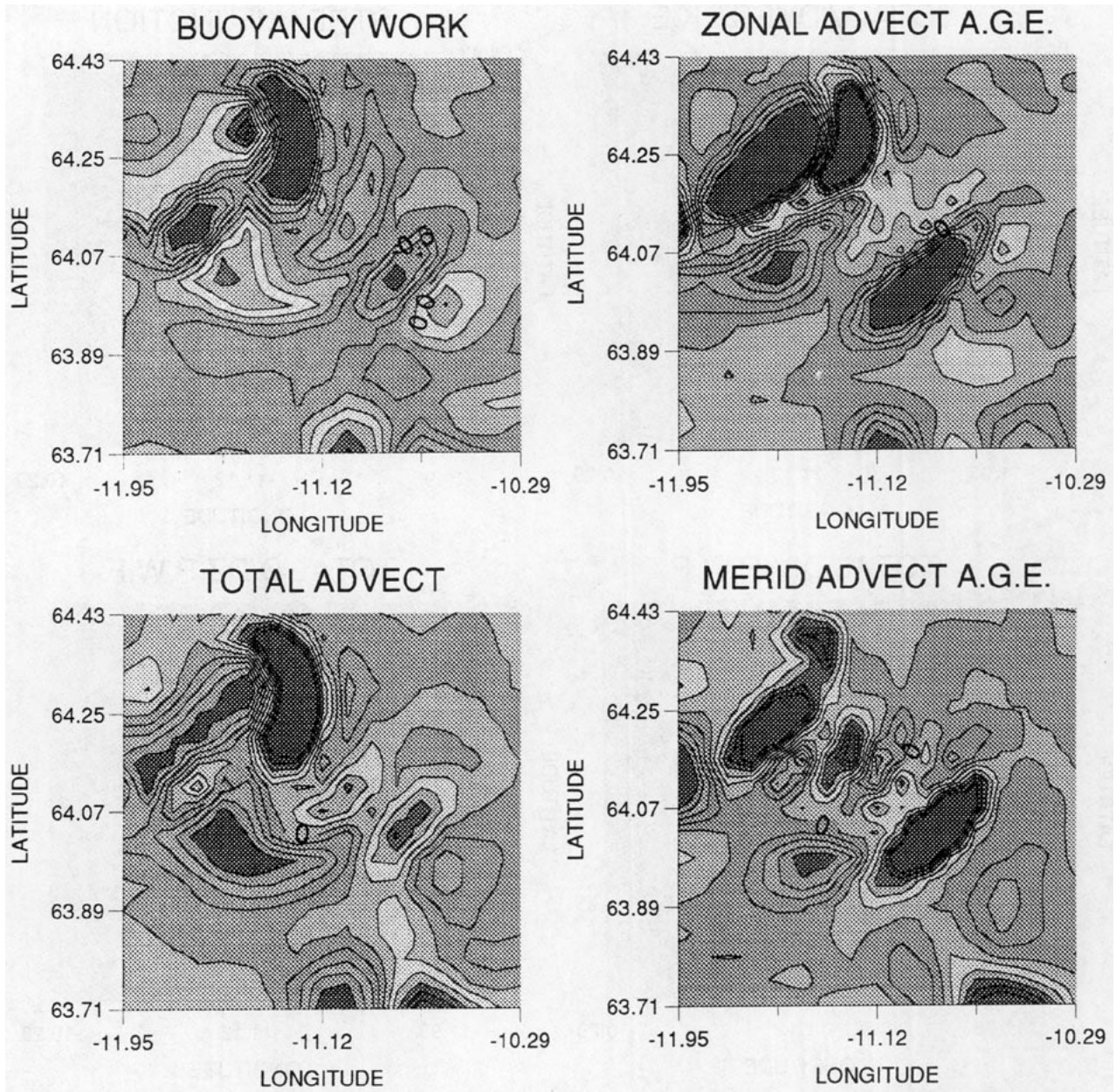
FIG. 17. Case BC4X subdomain spatial fields of b, ΔF_A, and the zonal and meridional components of ΔF_A from the AGE equation for level 3 and day 3 of the forecast. Contour interval is 0.5 nondimensional units (following Pinardi and Robinson 1986). Shading scale is chosen to highlight positive regions that are light for small values then dark for large values, while negative regions are grey for small negative values then dark for large negative values.

will now show that the cold tongue intrusion event is clearly associated with baroclinic instability.

Consider only an $(80 \text{ km})^2$ portion of the total model domain surrounding the developing cold tongue intrusion for case BC4X (Fig. 1b). Figure 16 shows averages over this subdomain of key terms at selected levels in the AGE and KE equations. For example, during the strong growth phase of the cold intrusion (day 2–3), at middepth (250 m) the buoyancy coupling term in Fig. 16a is negative, indicating a transfer of energy from

potential to kinetic energy. At that same level in the KE equation (Fig. 16b), the average vertical pressure transfer is negative. Since that term is positive in the two upper layers (e.g., Fig. 16c), it clearly indicates a transfer of energy upwards from the buoyancy coupling source. This entire scenario is clearly similar to the Eady baroclinic instability case discussed by Pinardi and Robinson (1986). In contrast, the basic signature of the barotropic instability case is not evident in these balances.
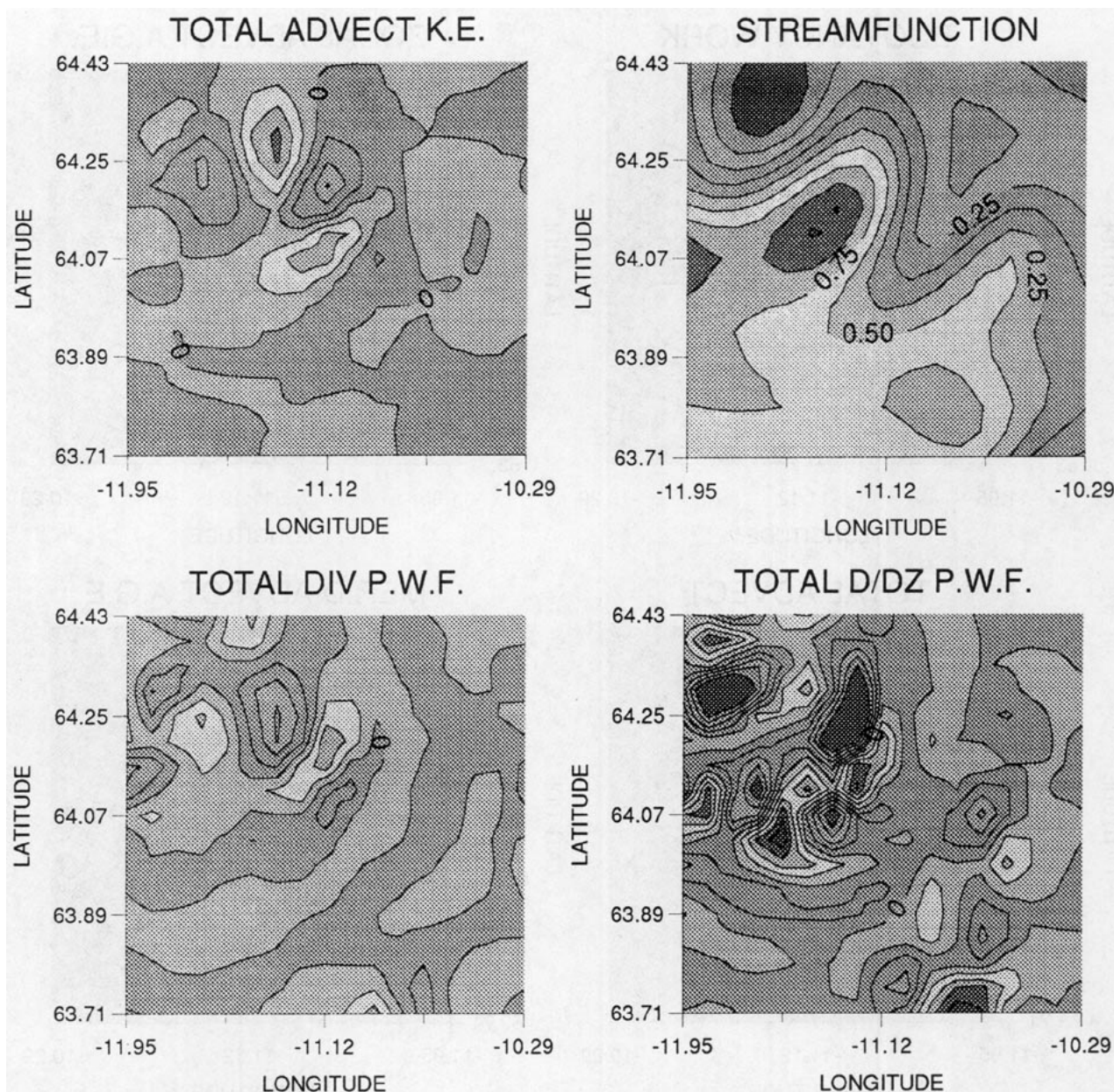
FIG. 18. Case BC4X subdomain spatial fields of ΔF_K, ΔF_π, ψ, and δf_π from the KE equation for level 3 and day 3 of the forecast. Contour interval is 1.0 nondimensional unit for the energy terms and 0.25 for ψ. Otherwise, as in Fig. 17.

Since the above averages correspond to a rather large area surrounding the developing cold tongue, consider further the spatial plots of the key terms in the energy equations. Figure 17 shows the buoyancy and advection terms for the AGE equation for level 3 (250-m depth) on day 3 of the BC4X forecast. In the vicinity of the cold tongue intrusion (which is indicated in the streamfunction plot in Fig. 18), one can see that the buoyancy coupling term is negative, with maxima on either side of the developing cold tongue (Fig. 17). The total advection, in contrast, is positive in the region of the cold tongue, indicating energy being drawn from

the mean vertical shear of the water column. A similar pattern occurs at level 4 (400 m).

Figure 18 shows level 3 (250 m) for key terms in the KE equation. In the region around the developing cold tongue, the vertical pressure working rate results in a net extraction of energy. A similar effect occurs in the warm meander in the north-central part of the subdomain. Here F_κ and F_π are relatively unimportant at this depth. In the top layer (Fig. 19), in contrast, buoyancy work has little effect and the vertical pressure working rate acts as the primary energy source. The redistribution of energy due to horizontal KE advection
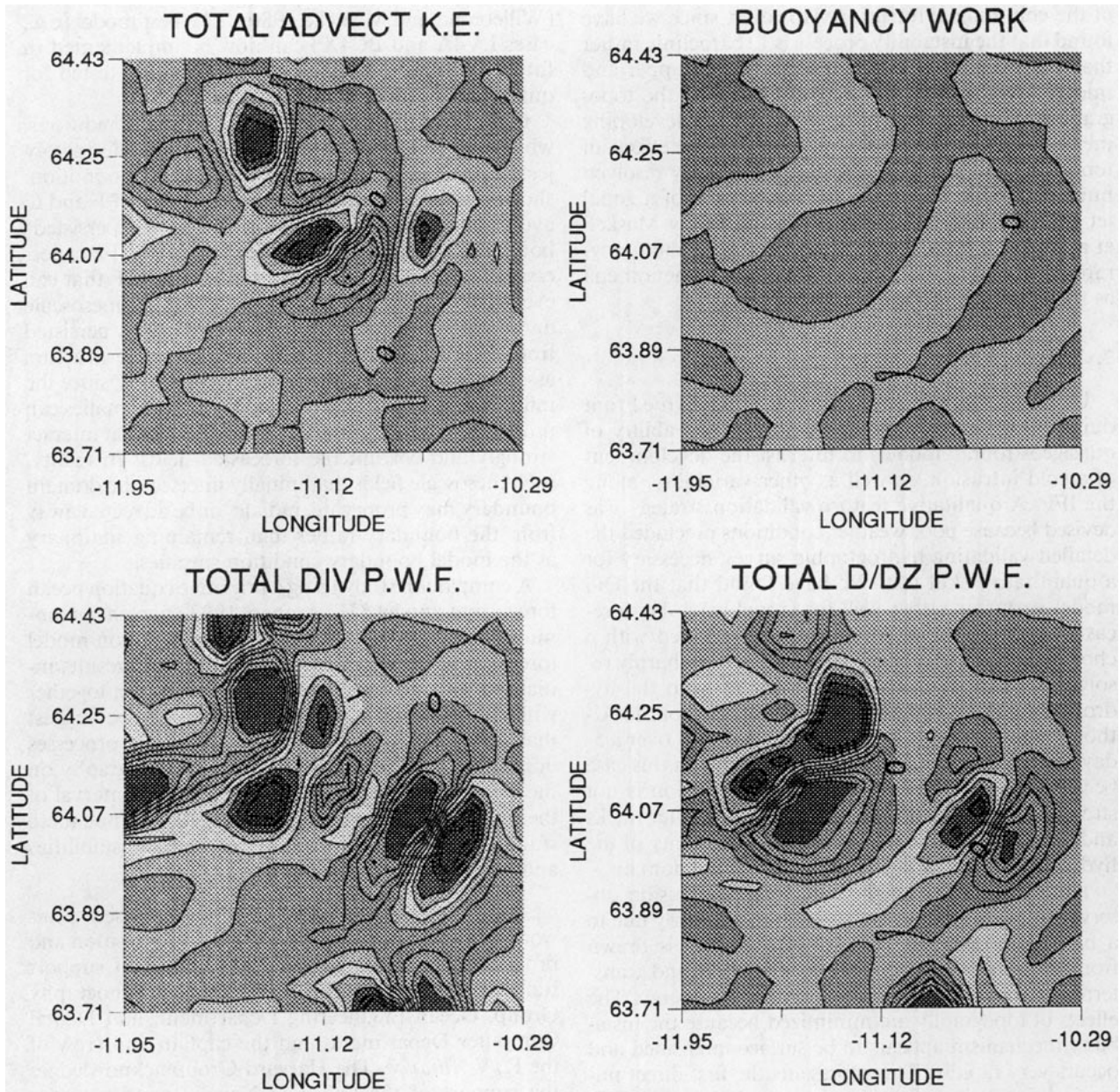
FIG. 19. Case BC4X subdomain spatial fields of ΔF_K, ΔF_π, b, and δf_π from the KE equation for level 2 and day 3 of the forecast.
Otherwise as in Fig. 18.

and horizontal pressure work is a large and complicated field at this level around the developing instability.

This analysis clearly reveals the importance of the buoyancy conversion term at middepth, indicative of a baroclinically unstable flow during the first three days of the forecast. The structure of the energetic transfers in the middle and upper water column also point to baroclinic rather than barotropic instability processes. We have performed an analogous energy equation analysis for several other model cases to address the sensitivity of this result. These included the model jet case 3 (JM4-4) and the 400-m level of no motion case

with full topography (LV4AT). The results of neither case deviate significantly from those just discussed. Furthermore, our results are consistent with the statistical analysis of temperature and velocity fluctuations in the IFF by Willebrand and Meincke (1980) that showed strong conversion of available potential energy to eddy kinetic energy, suggestive of baroclinic instability (cf., Allen et al. 1994).

Although the establishment of the observed initial state certainly has been influenced by past effects of topographic interaction, it is surprising that the effect of topography is rather minor in the rapid development

of the cold tongue intrusion. However, since we have found that the instability process is 1) baroclinic rather than barotropic and 2) most active in the upper and middle levels of the model, it is clear why the topographic effect fails to strongly influence the developing meanders. A similarly weak influence of the effects of topography in the first several days of eddy-resolved numerical experiments on the breakdown of a zonal jet over IFF-like topographies was found by Maskell et al. (1992), although after about a week the topography had paramount importance in such phenomena as their simulated bottom-trapped eddies.

7. Summary and discussion

Using data gathered around the Iceland–Faroe Front during October 1992, we have studied the ability of quasigeostrophic models to forecast the development of a cold intrusion, as well as other variability, along the IFF. A qualitative feature validation strategy was devised because poor weather conditions precluded the detailed validating hydrographic survey necessary for a quantitative skill test. We have found that the QG model performs rather well for (roughly) 4-day forecasts when the initial conditions are specified with a choice of objective analysis parameters that sharply resolves the frontal structure determined from the hydrocast dataset using a 400-m level of no motion. Although these initial conditions were gathered over a 5-day period, they can be treated as synoptic in this case because the development of the cold intrusion is not strongly affected by upstream variability. Drifter tracks and satellite images corroborate the synopticity of the hydrocast survey in the western part of the domain.

The rapid growth of the cold tongue intrusion observed along the IFF was diagnosed to be clearly due to a baroclinic instability mechanism. Energy is drawn from the mean vertical shear at middepth and transferred to the mid- and upper-level kinetic energy. The effects of topography are minimized because the instability mechanism appears to be surface intensified and occurs very rapidly. This represents the first direct numerical simulation of an observed instability in the IFF.

Due mainly to a lack of verifying datasets, statistical validations of QG forecasts (e.g., Robinson et al. 1984; Denbo et al. 1988; Denbo and Robinson 1988a; Robinson et al. 1989; Glenn et al. 1991) are difficult. We have shown here that a feature validation technique can be used for model validation in lieu of sufficient data for a rigorous statistical error analysis. But it must be noted that, since there are many ways to vary the model output and only a few matching criteria, it might be possible to match the validation features even with inaccurate dynamics. Nonetheless, the best forecasts in this study validate against all three features (cold tongue intrusion, current disappearance, and northward shift of the IFF), and the results of the physical process study are consistent with previous research

(Willebrand and Meincke 1980). The best model (e.g., cases LV4A and BC4X) can now be implemented in future IFF QG forecasting expeditions and tested for quantifiable skill (e.g., Miller et al. 1995).

Our exploration of the effects of initial conditions, which can be altered simply by choosing differing objective analysis parameters and/or level of no motion, shows that it is vital to properly resolve the IFF and to avoid generating excessive structure in the (persisted) boundary conditions. The resolution of the IFF is necessary to retain seed perturbations in the IFF that can eventually grow to become significant mesoscale anomalies. The boundary conditions, when persisted from their initial state, should avoid excessive structure associated with ambient mesoscale variations, since the inflow/outflow currents implied by such anomalies can produce flows in the interior of the domain that interact strongly and corrupt the forecasted fields. In reality, such mesoscale fields that initially intersect the domain boundary may propagate, radiate, or be advected away from the boundary rather than remaining stationary as the model boundary condition specifies.

A companion study using a primitive equation ocean forecasting model (H. Arango 1993, personal communication) shows that the primitive equation model forecast has many similarities with the QG results initialized with similarly smoothed fields. Taken together with the energetic diagnosis of this study we suggest that surface-intensified baroclinic instability processes dominate over the effects of wind and topography on the evolving IFF structure during the time interval of these surveys. It would be interesting to continue these studies during other realizations of frontal instabilities and at other times of year.

REFERENCES

Allen, J. T., D. A. Smeed, and A. L. Chadwick, 1994: Eddies and mixing at the Iceland–Faroes Front. *Deep-Sea Res.,* **41,** 51–79.

Bennett, A. F., and M. A. Thorburn, 1992: The generalized inverse of a nonlinear quasigeostrophic general circulation model. *J. Phys. Oceanogr.,* **22,** 213–230.

——, L. M. Leslie, C. R. Hagelberg, and P. E. Powers, 1993: Tropical cyclone prediction using a barotropic model initialized by a generalized inverse method. *Mon. Wea. Rev.,* **121,** 1714–1729.

Carter, E. F., and A. R. Robinson, 1987: Analysis models for the estimation of oceanic fields. *J. Atmos. Oceanic Technol.* **4,** 49–74.

Denbo, D. W. and A. R. Robinson, 1988a: Harvard gapcasts. A progress report: Regional forecasting, processes and methodology in the East Iceland–Faroe Front. Part I: Data, forecast and hindcast experiments. Reports in Meteorology and Oceanography No. 32, Harvard University, Cambridge, MA, 203 pp.

——, and ——, 1988b: Harvard gapcasts. A progress report: Regional forecasting, processes and methodology in the East Iceland–Faroe Front. Part II: GFD and process experiments. Reports in Meteorology and Oceanography No. 33, Harvard University, Cambridge, MA, 218 pp.

——, R. A. Schmalz, and G. Gardner, 1988: Harvard gapcasts. Dynamical nowcasts and forecasts of the East Iceland–Faroe Front. Reports in Meteorology and Oceanography No. 30, Harvard University, Cambridge, MA, 203 pp.

Glenn, S. M., D. L. Porter, and A. R. Robinson, 1991: A synthetic geoid validation of Geosat mesoscale dynamic topography in the Gulf Stream region. *J. Geophys. Res.,* **96,** 7145–7166.

Haidvogel, D. B., A. R. Robinson, and E. E. Schulman, 1980: The accuracy, efficiency and stability of three numerical models with application to open ocean problems. *J. Comput. Phys.,* **34,** 1–53.

Hansen, B. and J. Meincke, 1979: Eddies and meanders in the Iceland–Faroe Ridge area. *Deep-Sea Res.,* **26,** 1067–1082.

Hopkins, T. S., 1991: The GIN Sea—A synthesis of its physical oceanography and literature review 1972–1985. *Earth-Sci. Rev.,* **30,** 175–318.

Maskell, S. J., A. D. Weathershaw, and C. E. Stretch, 1992: Topographic and eddy effects in a primitive equation model of the Iceland–Faeroes Front. *J. Mar. Sys.,* **3,** 343–380.

Miller, A. J., P.-M. Poulain, A. R. Robinson, H. G. Arango, W. G. Leslie, and A. Warn-Varnas, 1995: Quantitative skill of quasigeostrophic forecasts of a baroclinically unstable Iceland–Faroe front. *J. Geophys. Res.,* in press.

Miller, R. N., A. R. Robinson, and D. B. Haidvogel, 1981: A baroclinic quasigeostrophic open ocean model. *J. Comput. Phys.,* **50,** 38–70.

Millif, R. F., and A. R. Robinson, 1992: Structure and dynamics of the Rhodes Gyre System and dynamical interpolation for estimates of the mesoscale variability. *J. Phys. Oceanogr.,* **22,** 317–337.

Mooers, C. N. K., A. R. Robinson, and J. D. Thompson, Eds., 1986: *Proc. of the Ocean Prediction Workshop,* Phase I and II, Office of Naval Research.

Niiler, P. P., S. Piacsek, L. Neuberg, and A. Warn-Varnas, 1992: Sea surface temperature variability of the Iceland–Faeroes Front. *J. Geophys. Res.,* **97,** 17 777–17 785.

Özsoy, E., C. J. Lozano, and A. R. Robinson, 1992: A consistent baroclinic quasigeostrophic ocean model in multiply connected ocean domains. *Math. Comput. Sim.,* **34,** 51–79.

Peloquin, R. A., and Collaborators, 1992: Ocean modeling and prediction, *Oceanography,* **5** (Special Vol.), 4–77.

Perkins, H., 1992: Large-scale structure of the Iceland–Faroe Front. SACLANT Undersea Research Centre Rep. SR-189, La Spezia, Italy, 40 pp.

Pinardi, N., and A. R. Robinson, 1986: Quasigeostrophic energetics of open ocean regions. *Dyn. Atmos. Oceans,* **10,** 185–219.

Poulain, P.-M., 1992: Cruise Rep. for R/V *Alliance:* GIN92, Greenock-Liverpool, 13–29 October, 1992. [Available from SACLANT Undersea Research Centre, 19138 La Spezia, Italy.]

——, and A. Warn-Varnas, 1993: Hydrographic, satellite and drifter observations in the Iceland-Faroe frontal region in October 1992. *Ann. Geophys.,* **11** (Suppl II), C158 (abstract).

Robinson, A. R., 1992: Shipboard prediction with a regional forecast model. *Oceanography,* **5,** 42–48.

——, and W. G. Leslie, 1985: Estimation and prediction of oceanic eddy fields. *Progress in Oceanography,* Vol. 14, Pergamon Press, 485–510.

——, and L. J. Walstad, 1987: The Harvard Open Ocean Model: Calibration and application to dynamical process, forecasting, and data assimilation studies. *Appl. Num. Math.,* **3,** 89–131.

——, J. A. Carton, C. N. K. Mooers, L. J. Walstad, E. F. Carter, M. M. Rienecker, J. A. Smith and W. G. Leslie, 1984: A real time dynamical forecast of ocean synoptic/mesoscale eddies. *Nature,* **309,** 5971–5972.

——, S. M. Glenn, M. A. Spall, L. J. Walstad, G. M. Gardner, and W. G. Leslie, 1989: Forecasting Gulf Stream meanders and rings. *Eos,* **70,** 1464–1473.

Scott, J. C., and A. L. McDowall, 1990: Cross-frontal cold jets near Iceland: In-water, satellite infrared and GEOSAT altimeter data. *J. Geophys. Res.,* **95,** 18 005–18 014.

Smart, J. H., 1984: Spatial variability of major frontal systems in the North Atlantic Norwegian Sea area: 1980–1981. *J. Phys. Oceanogr.,* **14,** 185–192.

Spall, M. A., and A. R. Robinson, 1990: Regional primitive equation studies of the Gulf Stream meander and ring formation region. *J. Phys. Oceanogr.,* **20,** 985–1016.

Warn-Varnas, A., L. Henderson, P. Van Meurs, and S. Piacsek, 1993: Diagnostic modelling studies of the Iceland–Faroe Front. SACLANT Undersea Research Centre Rep. SR-204, La Spezia, Italy, 39 pp.

Willebrand, J., and J. Meincke, 1980: Statistical analysis of fluctuations in the Iceland–Scotland frontal zone. *Deep-Sea Res.,* **27A,** 1047–1066.